minerals

MDPI

Article

# Post-Mineralization, Cogenetic Magmatism at the Sungun Cu-Mo Porphyry Deposit (Northwest Iran): Protracted Melting and Extraction in an Arc System

**Amin Allah Kamali [1], Mohsen Moayyed [1,*], Nasir Amel [1], Mohammad Reza Hosseinzadeh [1], Kourosh Mohammadiha [2], José Francisco Santos [3] and Marco Brenna [4]**

1 Department of Earth Sciences, Faculty of Natural Sciences, University of Tabriz, Tabriz 5166616471, Iran; aminkamali1984@gmail.com (A.A.K.); amelnasir@gmail.com (N.A.); mr-hosseinzadeh@tabrizu.ac.ir (M.R.H.)
2 Geological Survey & Mineral Explorations of Iran, Tehran 131851494, Iran; Mohammadiha@gsi.ir
3 Geobiotec, Department of Geosciences, University of Aveiro, 3810-193 Aveiro, Portugal; jfsantos@ua.pt
4 Department of Geology, University of Otago, Dunedin 9016, New Zealand; marco.brenna@otago.ac.nz
* Correspondence: Moayyed@tabrizu.ac.ir; Tel.: +98-41-33392621

Received: 5 July 2018; Accepted: 26 September 2018; Published: 12 December 2018


**Abstract:** The Sungun porphyry ore deposit is located in Eastern Azarbaijan province, Northwestern Iran. The oldest intrusive pulse in the region is a quartz-monzonite pluton, which hosts the porphyry copper-molybdenum mineralization. The Sungun Copper Mine includes the mineralized Sungun porphyry as well as six groups of cross-cutting and lithologically distinct post-mineralization dykes. The composition of these dykes ranges from quartz diorite, gabbro, diorite, dacite, lamprophyre, and microdiorite. Quartz diorite and dacite dykes are the oldest and youngest dykes, respectively. Based on their cross-cutting relationships, the composition of the dykes tend to become more primitive through time. The dykes strike Northwest–Southeast with Southwest dip, sub-parallel to the reverse faults within the deposit area. The lamprophyric dykes range from phonotephrite, to trachybasalt, tephrite, and basanite. The quartz-monzonite porphyry (SP) and the post-mineralization dykes (DK1-DK3) have clear and distinct negative anomalies of Ti, Zr, P, Pr, Ce, and Nb, as well as positive anomalies of Cs, U, K, Pb, and Nd with respect to primitive mantle. Microdioritic dykes (MDI) show depletion of Ti, Nb, P, Ta, Th, Yb, and Zr, and enrichment of Cs, Ba, U, Pb, Nd. The similarities in trace element abundances and patterns in the porphyry and post-mineralization calc-alkaline dykes implies a single source and fractional crystallization as the main mechanism controlling magmatic evolution in a collisional environment. Lamprophyric dykes have enrichment of LREE and LILE and depletion of HREE and HFSE such as Ti, Nb, and Ta. The parent magma of the lamprophyric dykes (LAM) was likely derived by low degrees of melting of a garnet lherzolite mantle peridotite. The $^{87}Sr/^{86}Sr$ and $^{143}Nd/^{144}Nd$ ratios range from 0.704617 to 0.706464 and from 0.512648 to 0.512773 for the dykes suggesting that the parental magmas came from a progressively more enriched mantle. Isotope ratios of $^{87}Sr/^{86}Sr$ and $^{143}Nd/^{144}Nd$ support a cogenetic relationship of porphyry and calc-alkaline dykes, except for the microdiorite ones. A common primary melt underwent gravity differentiation in a deep magmatic chamber to form a dioritic magma. This subsequently migrated to shallower levels to evolve further and feed individual dyke groups into the Sungun porphyry.

**Keywords:** cogenetic magmatism; dioritic magma; post-mineralization dykes; Sungun; porphyry deposit

## 1. Introduction

The Sungun Cu-Mo porphyry is situated in the NW-trending part of the Central Iran post-collisional magmatic arc zone [1] known as Sahand–Bazman (Figure 1). Porphyry copper deposits

form along convergent plate boundaries in continental magmatic arcs or in island-arc environments [2]. These deposits are associated with subduction-related volcanic centers, although in some examples, they are thought to be associated with post-collisional volcanism [2]. Giant porphyry copper deposits in Iran and Pakistan occur in a region along the suture zone between the Arabian (Afro-Arabian) and Eurasian plates following subduction of the Neo-Tethys oceanic plate [3]. Reference [4] noted that continental arc-style magmatism related to the subduction of the Neo-Tethys oceanic plate produced several porphyry deposits such as the porphyry copper-molybdenum deposit at Sungun (northwestern Iran), the giant gold-rich porphyry copper deposit at Sarcheshmeh, and porphyry copper deposit at Meiduk. The magmatic suites in this area are part of the NW–SE trending Cenozoic magmatic belt of Iran and the porphyries occur as stocks and dykes [5,6] (Figure 1).

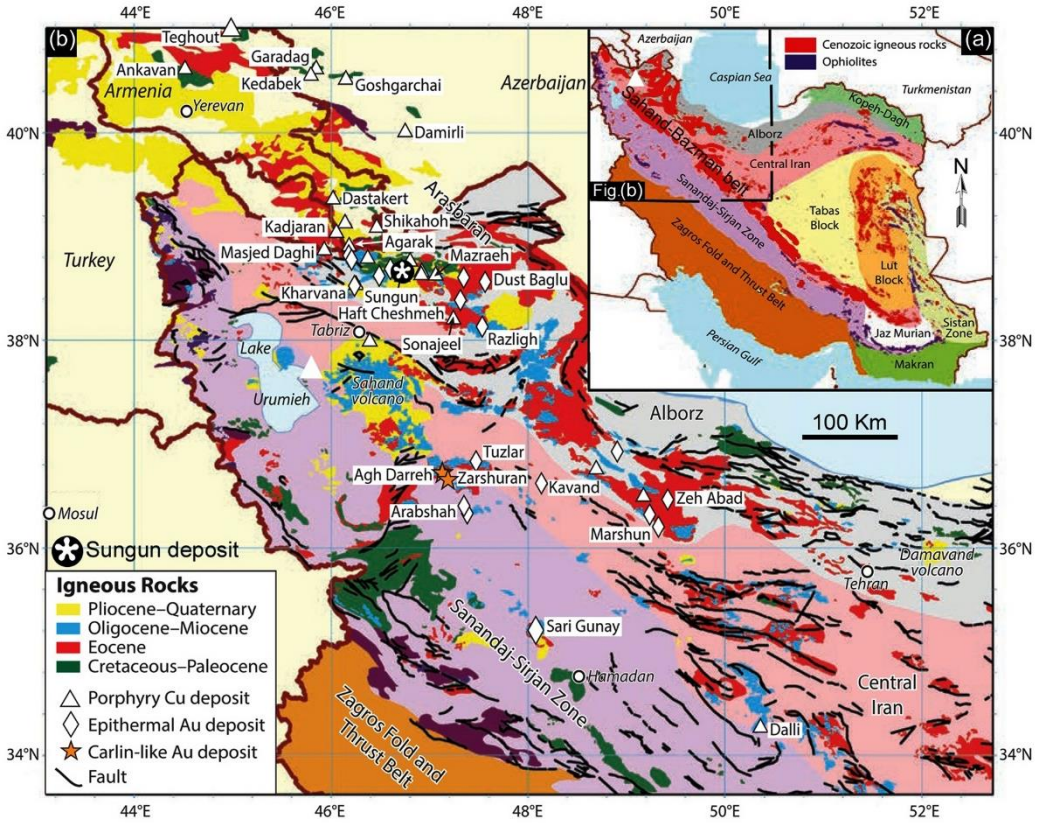


**Figure 1.** (**a**) Main tectonic terranes of Iran and neighboring countries. Additionally mapped are late Mesozoic and Cenozoic magmatic provinces as well as ophiolitic domains [1,7]; (**b**) geologic map of Northwestern Iran, showing the locations of Mesozoic and Cenozoic igneous rocks and associated porphyry, epithermal, and Carlin-like deposits [7]. The location of the Sungun porphyry Cu-Mo deposit in the Sahand-Bazman belt is shown by a star [8].

Most porphyry copper deposits are associated to shallow-intermediate silicic intrusive complexes composed of small plutons and dykes. Some are associated solely to dykes. Porphyry Cu deposits are centered in porphyry intrusions that range from vertical, pluglike stocks, and are circular to elongate in a map view due to dyke arrays forming small, irregular bodies [9]. The stocks and dykes commonly have diameters and lengths of $\leq$1 km.

In most porphyry deposits around the world dyke suites have compositions associated to mineralized porphyry and are hence genetically related. In the copper belt of Iran, late and unmineralized dykes genetically related with the mineralized porphyry occur at Sarcheshmeh, Sara, Haftcheshmeh and Darrehzar [10–13]. The majority of studies on the Sungun porphyry Mo-Cu deposit consist of exploration companies reports alongside master and PhD dissertations, and focused on surveying the deposit geometry as well as determining the mechanisms of mineralization [14–27].

A quantitative study of the petrology and geology on post-mineralization dykes has yet to be conducted. In this paper we introduce new petrography, geochemistry, and isotopic data of the Sungun stock and the associated post-mineralization dykes and discuss the links between the two.

Abbreviations used are as follows: Sungun porphyritic body (SP); Three phases of quartz dioritic dykes divided in terms of alteration and temporal relationships (DK1a, DK1b, DK1c); Gabbrodioritic dykes (DK2); Dioritic dykes (DK3); Dacitic dykes (DK4); Microdioritic dykes (MDI); Lamprophyric dykes (LAM); Skarn (SKR), and Hornfels (HFS).

## 2. Geological Setting

Cenozoic magmatism and associated Porphyry copper mineralization in Iran occur in the Sahand–Bazman belt. The Sungun porphyry deposit is approximately 100 km NE of Tabriz in NW Iran (Figure 1). The oldest rocks in the study area are a 500 m sequence of Cretaceous limestone with intercalations of shale (Figure 2) [15,17]. Fossils in this unit have an Upper Cretaceous (Campanian-Maastrichtian) age. The oldest intrusive pulse in the region and the host of copper and molybdenum mineralization is a quartz-monzonite porphyry (Sungun Porphyry, SP). The quartz-monzonite stock has been dated by Ar-Ar at about 20.69 $\pm$ 0.37 ($\pm$0.2$\sigma$) Ma [25] and by U-Pb zircon at about 21 $\pm$ 0.15 Ma [27]. A skarn zone to the North and East of the Sungun-Chay and Pakhir-Chay rivers related to the quartz monzonite stock hosts the Cu-Mo deposit at Sungun. A hornfels zone outcrops along the Eastern margin of the porphyry and appears abundantly in drill cores (Figure 2).

Post-mineralization dykes in the Sungun deposit can be subdivided according to chemical composition and relative age (Figure 3). We characterized six dyke groups: (1) Quartz dioritic; (2) Gabbroic; (3) Dioritic; (4) Microdioritic; (5) Lamprophyric; and (6) Dacitic. Temporally, the dykes are further classified into eight categories, with the oldest being the DK1a quartz dioritic dykes and the youngest the dacite dykes (Figure 3).

Dykes are very strongly altered with most of the plagioclase megacrysts largely replaced by sericite, epidote, kaolinite, and carbonate. The width of the dykes varies from a few centimeters to approximately 30 m. The dykes show sharp, chilled contacts with the host rocks. The strike of the dykes, as measured in the field (N = 752), is generally similar to the trends of lineaments measured from aerial images. The field measurements show a somewhat more NW-SE trend of the dykes (Figure 4a,b).

Based on the appearance and cross-cutting relationships between the intrusions, three kinds of quartz-dioritic dykes were distinguished. The first generation is DK1a. They are light grey in colour and are generally very wide (0.5–20 m). References [25,27] reported an average age of 20.57 $\pm$ 0.45 Ma and 19.85 $\pm$ 0.33 Ma (U-Pb method, zircon). DK1a are frequently cut by DK1b (Figure 5a).

The second quartz diorite dyke generation is DK1b. They are dark grey in color, generally thinner and shorter than DK1a. In the mine pit DK1b are abundantly exposed with lengths ranging between 30 m and 3 km. They are easily recognizable by their coarse and pink orthoclase phenocrysts. DK1b dykes contain enclaves (Figure 5c) that can be divided into two groups: Dioritic enclaves and microgranular enclaves with quartz dioritic composition. The diameter of enclaves varies from a few millimeters to 30 centimeters (Figure 5c).

DK1c is the third and youngest generation compared to DK1a and DK1b, based on cross cutting relationships. The grey color of DK1 is clearly different from all of the other rocks of the units at Sungun, making them easily recognizable in the field.

Gabbroic dykes (DK2) have not been seen inside the Sungun deposit but are found on its Northeastern side. Gabbroic rocks (DK2) are dark grey in colour. This dyke group cuts quartz-diorite dykes and is cut by the diorite dykes (DK3). The diorite dykes (DK3) are younger than the quartz-diorite (DK1) and gabbroic dykes (DK2), and contain abundant hornfels enclaves (Figure 5d). These dykes can be seen in drill cores and outcrop in the Skarn portion.

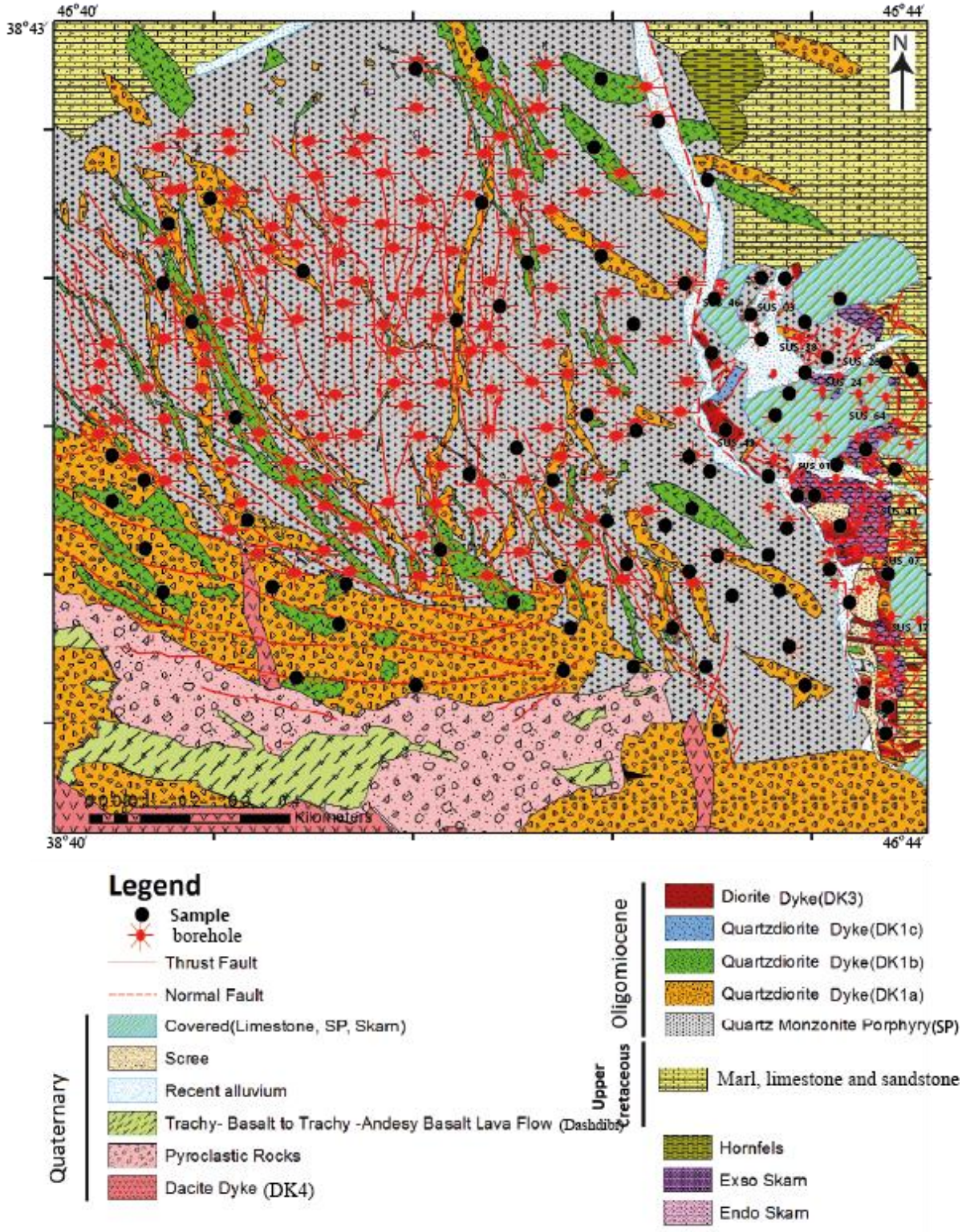


**Figure 2.** Geological map of the Sungun Copper Mine [28].

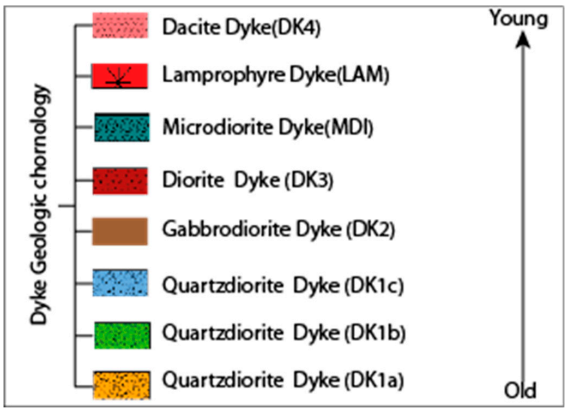


**Figure 3.** Classification of post-mineralization dykes is based on relative intrusive age.

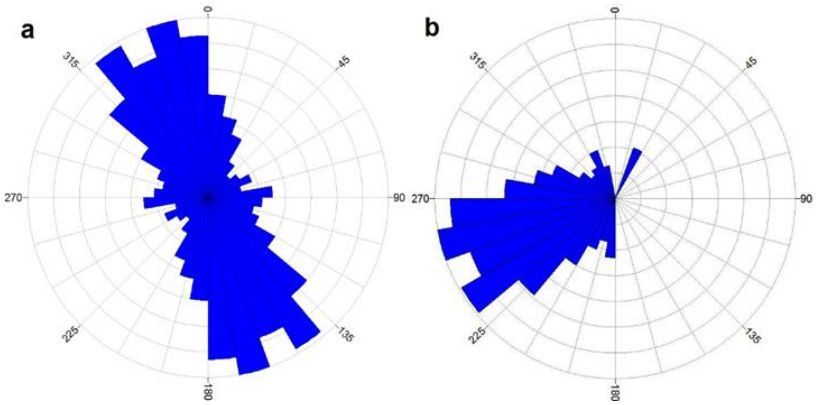


**Figure 4.** (**a**) Dykes trend in Sungun copper deposit (N = 752); (**b**) Dip of dykes in Sungun copper deposit.


**Figure 5.** Field photographs. (**a**) Quartz diorite (DK1b) dykes intruded into the quartz diorite (DK1a), view to the North; (**b**) quartz diorite (DK1c) and diorite (DK3) dykes intruded into the skarn, view to the SE; (**c**) Irregular mingled contact between fine-grained enclave and medium-grained quartz diorite (DK1b); and (**d**) hornfels enclave within an outcrop of fine-grained diorite (DK3).

Lamprophyre and microdiorite dykes have formally been reported only from drill core observations (Figure 6) [29,30]. Small microdiorite dykes are common in the Eastern skarn and are found in drill cores SUS_01 (Figure 6a), 03, 07, 17, 41, 43, 44, 46, and 52 (Figure 2). At Sungun the microdiorite dykes cross cut quartz-diorite dykes DK1a and DK1b. Lamprophyre dykes (LAM) have not been reported at the surface but are found in drill cores SUS_24, 26, 38, 42, and 64 (Figure 6b). The samples of the lamprophyre dykes are light green and grey in colour, fine-grained, and with porphyritic textures.

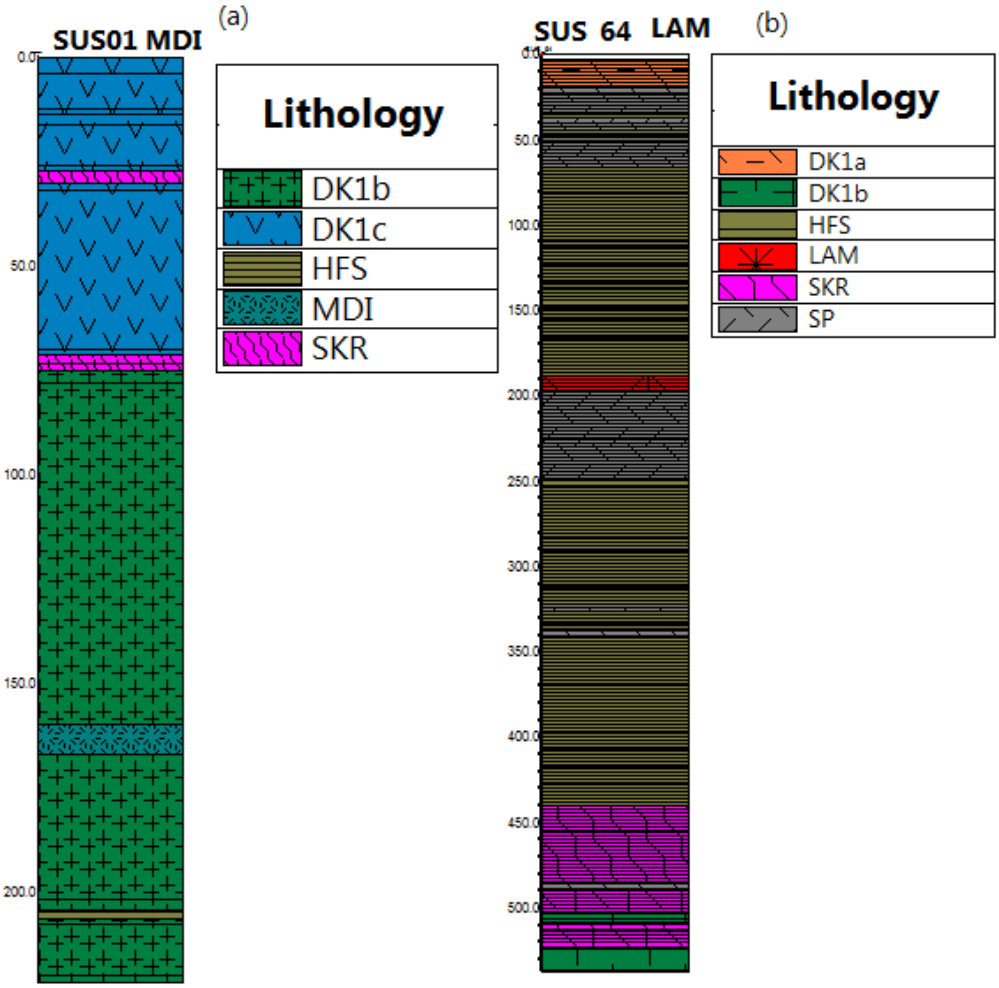


**Figure 6.** Two Sungun mine drill core logs representative of the diversisty of lithologies. (**a**) Core SUS01 contains a microdioritic dyke and (**b**) core SUS64 contains a lamprophyric dyke that have no surface exposure. SP is Sungun porphyry; DK1a, b and c are three phases of quartz dioritic dykes; DK2 is gabbrodiorite; DK3 is diorite; DK4 is dacite; MDI is a microdioritic dyke; LAM is a lamprophyric dyke; SKR is skarn; and HFS is hornfels.

Dacite dykes DK4 are related to Chaldaghi subvolcanic bodies, which have been attributed to the Plio-Quaternary [23]. These dacite dykes are covered by Plio-Quaternary epiclastic and pyroclastic rocks known as Dashdibi volcanics. Dacite dykes are grey to dark grey, fine grained, and containg mafic phenocrysts. Dacite dykes intrude the quartz monzonite of the Sungun porphyry. Dashdibi volcanics, as the latest and youngest episode of magmatism in the study area, cover approximately 2 $km^2$ of the altered SP quartz monzonite stock and post-mineralization dykes in the Southwest and West of Sungun. Dashdibi lavas are basaltic trachyandesite [23].

## 3. Materials and Methods

A total of 200 rock samples from various lithologies in the Sungun deposit (20-SP, 95-DK1, 5-DK2, 35-DK3, 5-DK4, 20-LAM, and 20-MDI) were collected, of which 100 thin sections were studied by a polarized microscope to identify the mineral assemblages. Twenty nine representative samples and an additional thirty six from [26] were selected for whole-rock chemical analysis. Samples were analyzed for major elements by X-ray fluorescence using standard XRF techniques. Trace and rare-earth elements were analyzed by Lithium borate fusion ICP-MS at the ALS-Chemex Laboratories, Vancouver, Canada. For mineral chemistry 6 sample thin sections including amphiboles, biotites and plagioclase were selected and analyzed using the CAMECA SX100 at the Oklahoma University Microprobe Laboratory. Typical beam operating conditions were 20 kV and 20 nA.

Six samples from the post-mineralization dykes were analysed for Sr and Nd isotopic compositions in the Laboratory of Isotope Geology of the University of Aveiro, Portugal. Powdered samples were dissolved by $HF/HNO_3$ solution in PTFE-lined Parr acid digestion bombs at a temperature of 180 °C for 3 days. After the final solution evaporation, the samples were dissolved in HCl (6.2 M) also in acid digestion bombs, and dried again. The elements analyzed were purified in two steps using conventional ion chromatography technique: Sr and REE elements separation in ion exchange columns was done using AG8 50 W cation exchange resin (Bio-Rad, Hercules, CA, USA); Nd separation from the other lanthanides was done with Ln cation exchange resin (Eichrom Technologies, Lisle, IL, USA). All reagents used in sample preparation were sub-boiling distilled and the water was produced by a Milli-Q Element System apparatus (Merck Millipore, Darmstadt, Germany). Strontium was loaded in a single Ta filament with $H_3PO_4$ whereas Nd was loaded on a Ta outer side filament with HCl in a triple filament arrangement. $^{87}Sr/^{86}Sr$ and $^{143}Nd/^{144}Nd$ isotopic ratios were determined using a multi-collector thermal ionization mass spectrometer (TIMS) VG Sector 54 device. Data were acquired in dynamic mode with peak measurements at 1–2 V for $^{88}Sr$ and 0.5–1.0 V for $^{144}Nd$. typical runs consisted of acquisition of 60 isotopic ratios. The isotopic ratios of Sr and Nd were corrected for mass fractionation relative to $^{88}Sr/^{86}Sr = 0.1194$ and $^{146}Nd/^{144}Nd = 0.7219$. During this study, the SRM-987 standard gave an average value of $^{87}Sr/^{86}Sr = 0.710249 \pm 12$ (conf. lim 95%, N = 12) and the JNdi-1 standard gave an average value of $^{143}Nd/^{144}Nd = 0.5121019 \pm 58$ (conf. lim 95%, N = 15).

## 4. Petrography

### *4.1. SP (Quartz-Monzonite)*

The main mineral associations in the Sungun porphyry deposit comprise plagioclase (40%–45%), orthoclase (30%–35%), amphibole (5%–10%), biotite (5%–10%), and quartz (5%–10%). Plagioclas is slightly altered to an assemblage of sericite, calcite and epidote (Figure 7a) in the propylitic zone and entirely decomposed to sericite in the phyllic zone. This mineral is fresh in the potassic zone and rarely altered to sericite. In the latter zone, metasomatic biotite is also observed. Ferromagnesian minerals such as amphibole and biotite are altered to a sericite-calcite-chlorite-epidote association in the propylitic zone and entirely replaced by sericite and opaque minerals and negligible chlorite and epidote in the phyllic zone. Accessory minerals comprise zircon, apatite, titanite, and opaque minerals (e.g., pyrite, chalcopyrite, magnetite, bornite, molybdenite, chalcocite, and covellite).

### *4.2. DK1 (Quartz Diorite)*

These dykes are dark gray to dark green in hand specimen and have massive texture. Post mineralization quartz diorite dykes in this region are subdivided into three categories based on alteration and relative emplacement age (DK1a, DK1b and DK1c).

#### 4.2.1. Dk1a

Quartz diorite dykes are composed mainly of plagioclase (50%–60%), biotite (15%–20%), amphibole (5%–10%), and accessory minerals which include K-feldspar, quartz, zircon, apatite, titanite,

and epidote (Figure 7b). Amphibole and biotite crystals are influenced by hydrothermal alteration and are locally completely altered to chlorite.

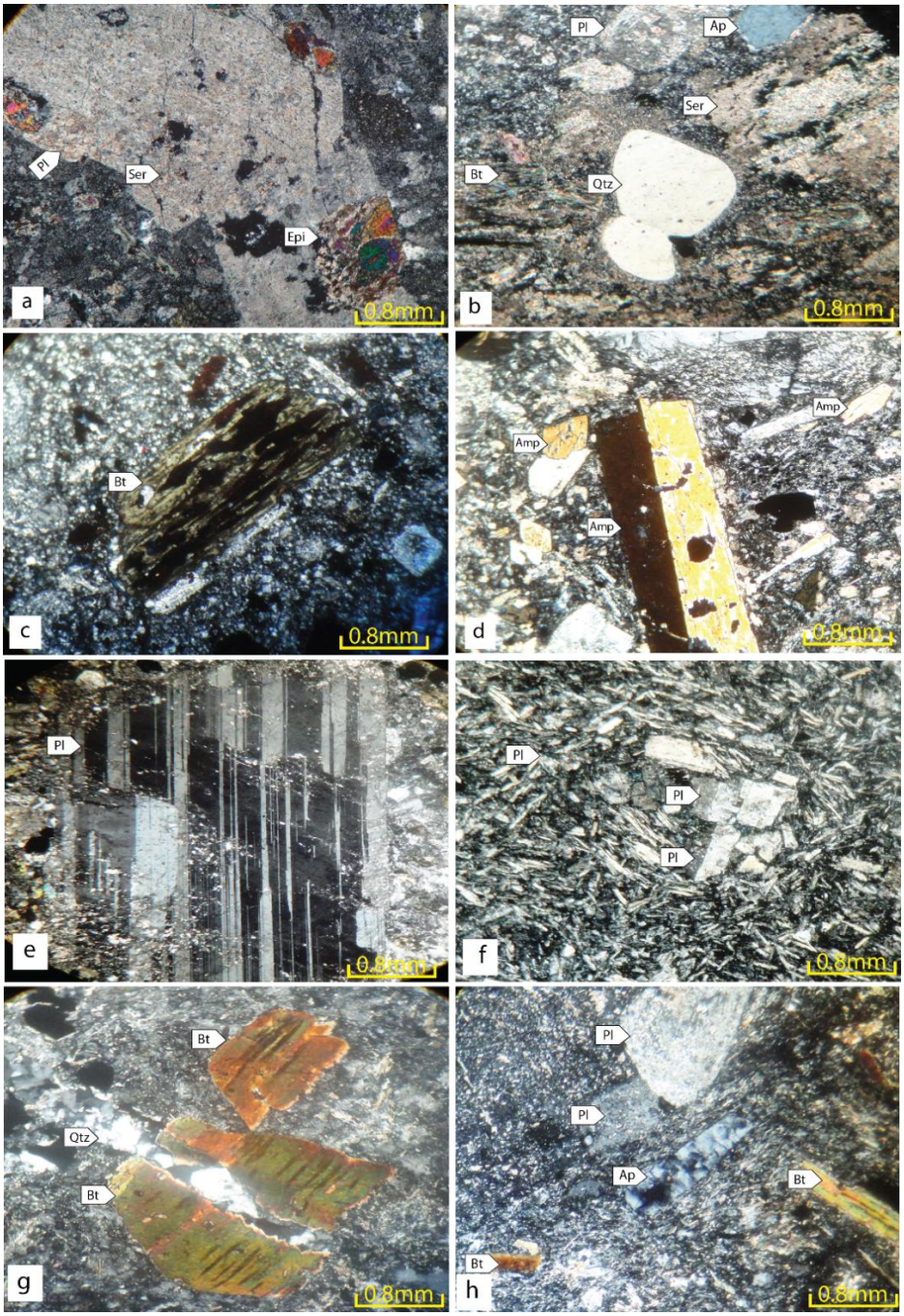


**Figure 7.** Photomicrographs (cross polarized light) show textures and mineral assemblages of the Sungun stock and post-mineralization dykes. (**a**) Alteration of plagioclase to sericite in quartz-monzonite; (**b**) subrounded "quartz eye" within altered plagioclase and biotite groundmass; quartz diorite dyke (DK1a); (**c**) Alteration of biotite to chlorite in quartz diorite; (**d**) amphibole with Carlsbad Twinning; (**e**) megacryst of plagioclase in diorite (DK3); (**f**) flow texture and cognate inclusion of feldspars in microdiorite (MDI); (**g**) megacryst of biotite in lamprophyre dyke; and (**h**) phenocryst of apatite in lamprophyre. Abbreviation: Amp = Amphibole, Chl = Chlorite, Am = amphibole, Bt = biotite, Pl = plagioclase, Ser = Sericite, Qtz = quartz, and Ap = apatite.

#### 4.2.2. DK1b

This rock is porphyritic with a microlithic porphyre textures groundmass and mainly consist of plagioclase, amphibole and biotite (Figure 7c). Plagioclase crystals mostly show alteration to sericite and epidote. Amphibole phenocrysts are partially altered to chlorite, but to a lesser degree than biotite, which is mostly altered to chlorite.

#### 4.2.3. DK1c

These dykes have dark green color. General textures are porphyritic with a microlithic groundmass. The quartz diorite consists of plagioclase, amphibole (Figure 7d), and biotite. Accessory minerals include quartz, titanite, and apatite.

### *4.3. DK2 (Gabbro)*

Gabbro commonly show a porphyritic texture with phenocrysts of pyroxene and plagioclase. Accessory phases are apatite, titanite, Fe-oxides, Fe-sulphides, and epidote.

### *4.4. DK3 (Diorite)*

These dykes are dark green and commonly show a porphyritic texture with phenocrysts consisting of plagioclase, amphibole, K-feldspar, and accessory phases including quartz, apatite, and titanite. Most plagioclases are altered to epidote, chlorite, and calcite, and K-feldspar is altered to sericite and clay minerals (Figure 7e). Amphibole is altered to chlorite and calcite.

### *4.5. DK4 (Dacite)*

These are dark grey in color and have porphyritic textures consisting of plagioclase and sanidine. Amphibole is an accessory mineral.

### *4.6. MDI (Microdiorite)*

Micro diorite is dark grey in color and commonly consists of phenocryst, groundmass, and cognate inclusions (Figure 7f). Phenocrysts mainly consist of feldspar and quartz.

### *4.7. LAM (Lamprophyre)*

In hand sample the color is gray to bright green. The rock is porphyritic with a microlitic groundmass. The main minerals include biotite (Figure 7g,h), amphibole, plagioclase, alkali feldspar, and pyroxene. Accessory minerals include apatite (Figure 7h), zircon, and quartz.

## 5. Mineral Chemistry and Whole Rock Geochemistry

### *5.1. Mineral Chemistry*

#### 5.1.1. Plagioclase

Representative compositions of plagioclase in Sungun deposit post-mineralization dykes, are reported in Table 1 and illustrated in Figure 8. Plagioclase in quartz diorite dykes (DK1) ranges from andesine to oligoclase with some nearly pure albite. Dacite dykes have the most anorthitic felsdspars, ranging from labradorite to andesine. Lamprophyre dykes contain oligoclase to albite, whereas microditorite dykes contain nearly pure albite.

**Table 1.** Representative microprobe analyses of plagioclases. Cations calculation is based on 8 oxygen.

| Sample | DK1a | | DK1b | | DK1c | | DK3 | | LAM | | MDI | |
|---|---|---|---|---|---|---|---|---|---|---|---|---|
| | a1 | a2 | b1 | b2 | c1 | c2 | k2 | k2 | L1 | L2 | M2 | M3 |
| $SiO_2$ | 68.71 | 68.56 | 62.75 | 61.94 | 58.93 | 57.42 | 56.41 | 56.56 | 68.92 | 68.77 | 67.7 | 66.77 |
| $TiO_2$ | 0 | 0 | 0 | 0 | 0 | 0 | 0 | 0 | 0 | 0 | 0 | 0 |
| $Al_2O_3$ | 20.43 | 20.19 | 21.71 | 20.73 | 25.1 | 26.95 | 26.83 | 26.36 | 20.46 | 20.51 | 20.05 | 20.41 |
| $Cr_2O_3$ | 0 | 0 | 0 | 0 | 0 | 0 | 0 | 0 | 0 | 0 | 0 | 0 |
| FeO | 0.03 | 0.03 | 0.59 | 0.56 | 0.25 | 0.24 | 0.41 | 0.42 | 0.01 | 0.01 | 0.2 | 0.07 |
| MnO | 0 | 0 | 0 | 0.01 | 0 | 0 | 0.01 | 0 | 0 | 0 | 0 | 0.03 |
| MgO | 0 | 0 | 0.44 | 0.44 | 0 | 0 | 0.02 | 0.03 | 0 | 0 | 0.05 | 0.02 |
| CaO | 0.11 | 0.09 | 2.7 | 4.13 | 7.02 | 8.3 | 9.65 | 9.25 | 0.57 | 0.57 | 0.45 | 0.23 |
| $Na_2O$ | 11.2 | 11.64 | 10.51 | 10.77 | 6.99 | 6.49 | 6.01 | 6.36 | 10.94 | 11.31 | 11.01 | 10.99 |
| $K_2O$ | 0.07 | 0.1 | 0.39 | 0.33 | 0.52 | 0.39 | 0.62 | 0.6 | 0.11 | 0.11 | 0.33 | 0.56 |
| Total | 100.55 | 100.6 | 99.09 | 98.91 | 98.81 | 99.79 | 99.96 | 99.58 | 101.01 | 101.28 | 99.79 | 99.08 |
| Si | 2.98 | 2.98 | 2.81 | 2.8 | 2.66 | 2.58 | 2.55 | 2.56 | 2.98 | 2.97 | 2.97 | 2.95 |
| Ti | 0 | 0 | 0 | 0 | 0 | 0 | 0 | 0 | 0 | 0 | 0 | 0 |
| Al | 1.04 | 1.03 | 1.15 | 1.11 | 1.34 | 1.43 | 1.43 | 1.41 | 1.04 | 1.04 | 1.04 | 1.06 |
| Cr | 0 | 0 | 0 | 0 | 0 | 0 | 0 | 0 | 0 | 0 | 0 | 0 |
| $Fe^{2+}$ | 0 | 0 | 0.02 | 0.02 | 0.01 | 0.01 | 0.02 | 0.02 | 0 | 0 | 0.01 | 0 |
| Mn | 0 | 0 | 0 | 0 | 0 | 0 | 0 | 0 | 0 | 0 | 0 | 0 |
| Mg | 0 | 0 | 0.03 | 0.03 | 0 | 0 | 0 | 0 | 0 | 0 | 0 | 0 |
| Ca | 0 | 0 | 0.13 | 0.2 | 0.34 | 0.4 | 0.47 | 0.45 | 0.03 | 0.03 | 0.02 | 0.01 |
| Na | 0.94 | 0.98 | 0.91 | 0.95 | 0.61 | 0.57 | 0.53 | 0.56 | 0.92 | 0.95 | 0.94 | 0.94 |
| K | 0 | 0.01 | 0.02 | 0.02 | 0.03 | 0.02 | 0.04 | 0.03 | 0.01 | 0.01 | 0.02 | 0.03 |
| Total | 4.97 | 5 | 5.08 | 5.13 | 4.99 | 5 | 5.02 | 5.03 | 4.97 | 4.99 | 4.99 | 5 |
| Or | 0.43 | 0.55 | 2.09 | 1.64 | 3.02 | 2.28 | 3.47 | 3.33 | 0.65 | 0.64 | 1.87 | 3.22 |
| Ab | 99.05 | 99.03 | 85.74 | 81.16 | 62.37 | 57.26 | 51.15 | 53.6 | 96.55 | 96.68 | 95.97 | 95.66 |
| An | 0.51 | 0.41 | 12.17 | 17.2 | 34.61 | 40.46 | 45.38 | 43.08 | 2.8 | 2.68 | 2.15 | 1.12 |

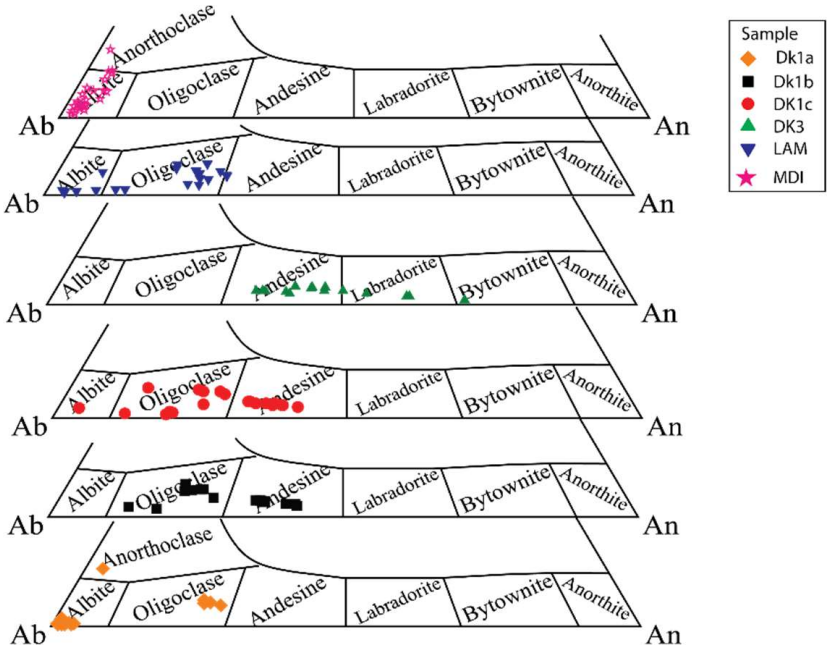


**Figure 8.** Plagioclases composition of dykes in the Sungun deposit classified based on the feldspar ternary diagram [31].

### 5.1.2. Amphibole

Representative compositions of amphiboles are presented in Table 2. Based on the $Mg/(Mg + Fe^{2+})$ vs. Si classification diagram, amphiboles from quartz diorite, diorite and lamprophyre dyke samples, plot in the fields of magnesiohornblende, and tschermakite (Figure 9). All amphiboles have between 6 and 7 Si atoms per formula unit (apfu), values which are typical of igneous amphiboles [32].

**Table 2.** Representative microprobe analysis of amphiboles in Sungun deposit late dykes. Cation calculation is based on 23 oxygen.

| Sample | DK1b | | | DK1c | | | DK3 | | | LAM | | |
|---|---|---|---|---|---|---|---|---|---|---|---|---|
| | b1 | b2 | b3 | c2 | c3 | c4 | 3.2 | 3.3 | 3.4 | L1 | L2 | L3 |
| $SiO_2$ | 46.81 | 46.67 | 46.66 | 46.04 | 46.72 | 46.59 | 43.26 | 47.85 | 47.36 | 46.28 | 45.68 | 44.64 |
| $TiO_2$ | 1.13 | 1.24 | 0.93 | 1.65 | 1.59 | 1.70 | 2.99 | 1.31 | 1.29 | 1.10 | 1.20 | 1.29 |
| $Al_2O_3$ | 7.96 | 8.53 | 8.67 | 8.77 | 8.35 | 8.53 | 10.56 | 7.02 | 7.29 | 7.90 | 8.13 | 8.79 |
| FeO | 14.70 | 15.39 | 15.39 | 13.97 | 12.62 | 12.68 | 12.02 | 11.50 | 11.57 | 14.13 | 14.65 | 15.23 |
| MnO | 0.32 | 0.38 | 0.37 | 0.13 | 0.10 | 0.08 | 0.24 | 0.33 | 0.34 | 0.33 | 0.34 | 0.30 |
| MgO | 13.36 | 13.59 | 13.61 | 13.41 | 14.11 | 13.96 | 14.52 | 16.45 | 16.18 | 13.86 | 13.37 | 13.06 |
| CaO | 11.43 | 11.44 | 11.27 | 12.62 | 12.94 | 12.65 | 11.25 | 10.51 | 10.59 | 11.24 | 11.14 | 11.27 |
| $Na_2O$ | 1.72 | 1.44 | 1.43 | 1.76 | 1.81 | 1.91 | 2.52 | 1.34 | 1.43 | 1.41 | 1.57 | 1.68 |
| $K_2O$ | 1.02 | 1.06 | 1.02 | 0.07 | 0.06 | 0.04 | 1.02 | 0.40 | 0.41 | 0.87 | 0.96 | 0.98 |
| Total | 100.53 | 101.85 | 101.46 | 100.51 | 100.40 | 100.24 | 100.48 | 98.82 | 98.56 | 99.19 | 99.10 | 99.30 |
| | | | | | | T | | | | | | |
| Si | 6.74 | 6.63 | 6.64 | 6.60 | 6.68 | 6.66 | 6.17 | 6.81 | 6.76 | 6.71 | 6.66 | 6.51 |
| Al(IV) | 1.26 | 1.37 | 1.36 | 1.41 | 1.32 | 1.34 | 1.77 | 1.18 | 1.23 | 1.29 | 1.34 | 1.49 |
| Ti | 0.00 | 0.00 | 0.00 | 0.00 | 0.00 | 0.00 | 0.06 | 0.02 | 0.01 | 0.00 | 0.00 | 0.00 |
| Total | 8.00 | 8.00 | 8.00 | 8.00 | 8.00 | 8.00 | 8.00 | 8.00 | 8.00 | 8.00 | 8.00 | 8.00 |
| | | | | | | C | | | | | | |
| Al(VI) | 0.09 | 0.05 | 0.09 | 0.08 | 0.08 | 0.10 | 0.00 | 0.00 | 0.00 | 0.06 | 0.05 | 0.02 |
| Ti | 0.12 | 0.13 | 0.10 | 0.18 | 0.17 | 0.18 | 0.26 | 0.12 | 0.13 | 0.12 | 0.13 | 0.14 |
| $Fe^{3+}$ | 0.96 | 1.11 | 1.17 | 0.99 | 0.86 | 0.88 | 1.31 | 1.25 | 1.26 | 1.07 | 1.10 | 1.23 |
| Mg | 2.87 | 2.88 | 2.89 | 2.86 | 3.01 | 2.98 | 3.09 | 3.49 | 3.45 | 3.00 | 2.90 | 2.84 |
| $Fe^{2+}$ | 0.81 | 0.72 | 0.66 | 0.69 | 0.64 | 0.63 | 0.12 | 0.12 | 0.12 | 0.65 | 0.69 | 0.63 |
| $Mn^{2+}$ | 0.04 | 0.05 | 0.05 | 0.02 | 0.01 | 0.01 | 0.03 | 0.02 | 0.04 | 0.04 | 0.04 | 0.04 |
| Total | 4.89 | 4.94 | 4.95 | 4.81 | 4.78 | 4.79 | 4.81 | 5.00 | 5.00 | 4.93 | 4.92 | 4.89 |
| | | | | | | B | | | | | | |
| Ca | 1.76 | 1.74 | 1.72 | 1.94 | 1.98 | 1.94 | 1.72 | 1.60 | 1.62 | 1.75 | 1.74 | 1.76 |
| Na | 0.24 | 0.26 | 0.28 | 0.06 | 0.02 | 0.06 | 0.28 | 0.37 | 0.38 | 0.25 | 0.26 | 0.24 |
| Total | 2.00 | 2.00 | 2.00 | 2.00 | 2.00 | 2.00 | 2.00 | 1.99 | 2.00 | 2.00 | 2.00 | 2.00 |
| | | | | | | A | | | | | | |
| Na | 0.24 | 0.14 | 0.11 | 0.43 | 0.48 | 0.47 | 0.42 | 0.00 | 0.02 | 0.14 | 0.18 | 0.24 |
| Ca | 0.00 | 0.00 | 0.00 | 0.00 | 0.00 | 0.00 | 0.00 | 0.00 | 0.00 | 0.00 | 0.00 | 0.00 |
| K | 0.19 | 0.19 | 0.19 | 0.01 | 0.01 | 0.01 | 0.19 | 0.07 | 0.08 | 0.16 | 0.18 | 0.18 |
| Total | 0.43 | 0.33 | 0.30 | 0.44 | 0.49 | 0.48 | 0.60 | 0.07 | 0.09 | 0.30 | 0.36 | 0.42 |

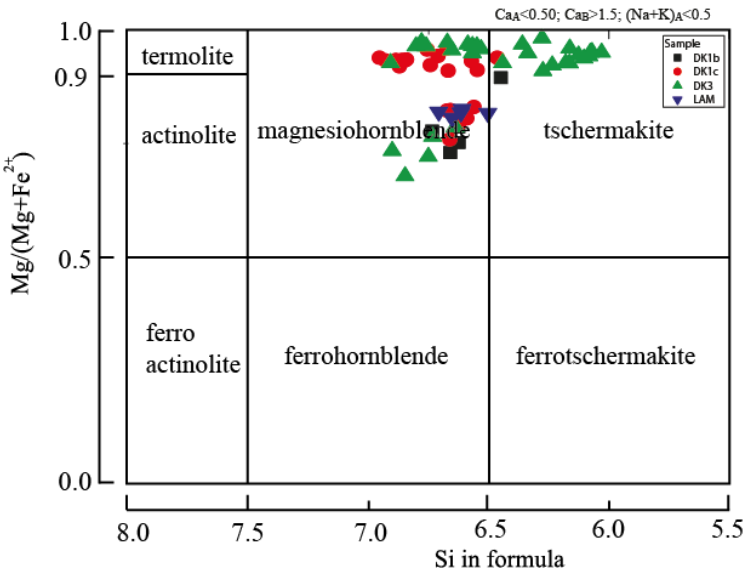


**Figure 9.** Major element data for amphiboles from dykes of the Sungun deposit plotted on the Mg/(Mg + $Fe^{2+}$) vs. Si classification diagrams [33].

### 5.1.3. Biotite

Representative biotite compositions are reported in Table 3. The biotites of quartz diorite and lamprohyre dykes generally do not show differences in chemical composition and are classified as Mg-rich biotite and phlogopite with XFe = $Fe^{2+}/Fe^{2+}$ + Mg) = 0.28–0.49 (Figure 10).

**Table 3.** Representative microprobe analysis of biotite. Cation calculation is based on 11 oxygen.

| Sample | DK1c | | | | LAM | | | |
|---|---|---|---|---|---|---|---|---|
| | **AB4** | **AB5** | **AB6** | **AB7** | **a1** | **a2** | **a3** | **a4** |
| $SiO_2$ | 37.56 | 37.37 | 36.88 | 36.49 | 38.14 | 38.06 | 37.95 | 37.98 |
| $TiO_2$ | 4.37 | 4.26 | 4.32 | 4.22 | 3.68 | 3.52 | 3.73 | 3.53 |
| $Al_2O_3$ | 14.2 | 14.3 | 14.13 | 14.12 | 14.86 | 14.4 | 14.41 | 14.52 |
| $Cr_2O_3$ | 0 | 0 | 0 | 0 | 0 | 0 | 0 | 0 |
| FeO | 13.66 | 13.85 | 13.48 | 13.5 | 16.13 | 16.16 | 16.21 | 15.19 |
| MnO | 0.14 | 0.15 | 0.13 | 0.15 | 0.08 | 0.08 | 0.07 | 0.06 |
| MgO | 16.56 | 16.4 | 15.51 | 15.6 | 14.94 | 14.6 | 14.55 | 15.2 |
| CaO | 0.03 | 0.04 | 0.01 | 0.02 | 0 | 0.01 | 0.02 | 0.01 |
| $Na_2O$ | 0.42 | 0.4 | 0.56 | 0.58 | 0.01 | 0.02 | 0.04 | 0.03 |
| $K_2O$ | 8.16 | 7.83 | 8.3 | 8.14 | 9.38 | 9.3 | 9.29 | 9.52 |
| BaO | 0 | 0 | 0 | 0 | 0 | 0 | 0 | 0 |
| F | 0.38 | 0.31 | 0.37 | 0.36 | 0.53 | 0.35 | 0.44 | 0.91 |
| Cl | 0.13 | 0.13 | 0.12 | 0.12 | 0.18 | 0.18 | 0.19 | 0.19 |
| O=F, Cl | 0.19 | 0.16 | 0.18 | 0.18 | 0.26 | 0.19 | 0.23 | 0.43 |
| Total | 95.8 | 95.2 | 93.99 | 93.48 | 98.19 | 96.87 | 97.13 | 97.53 |
| Formula 11(O) | | | | | | | | |
| Si | 2.77 | 2.77 | 2.78 | 2.76 | 2.79 | 2.81 | 2.8 | 2.8 |
| Ti | 0.24 | 0.24 | 0.24 | 0.24 | 0.2 | 0.2 | 0.21 | 0.2 |
| Al | 1.23 | 1.25 | 1.25 | 1.26 | 1.28 | 1.25 | 1.25 | 1.26 |
| Cr | 0 | 0 | 0 | 0 | 0 | 0 | 0 | 0 |
| $Fe^{3+}$ | 0.08 | 0.09 | 0.08 | 0.09 | 0.1 | 0.1 | 0.1 | 0.09 |
| $Fe^{2+}$ | 0.76 | 0.77 | 0.76 | 0.77 | 0.89 | 0.9 | 0.9 | 0.84 |
| Mn | 0.01 | 0.01 | 0.01 | 0.01 | 0 | 0.01 | 0 | 0 |
| Mg | 1.82 | 1.81 | 1.74 | 1.76 | 1.63 | 1.61 | 1.6 | 1.67 |
| Ca | 0 | 0 | 0 | 0 | 0 | 0 | 0 | 0 |
| Na | 0.06 | 0.06 | 0.08 | 0.08 | 0 | 0 | 0.01 | 0 |
| K | 0.77 | 0.74 | 0.8 | 0.79 | 0.87 | 0.88 | 0.88 | 0.9 |
| Ba | 0 | 0 | 0 | 0 | 0 | 0 | 0 | 0 |
| Total | 7.74 | 7.73 | 7.75 | 7.76 | 7.76 | 7.75 | 7.75 | 7.77 |
| Mg/Fe + Mg | 0.68 | 0.68 | 0.67 | 0.67 | 0.62 | 0.62 | 0.62 | 0.64 |

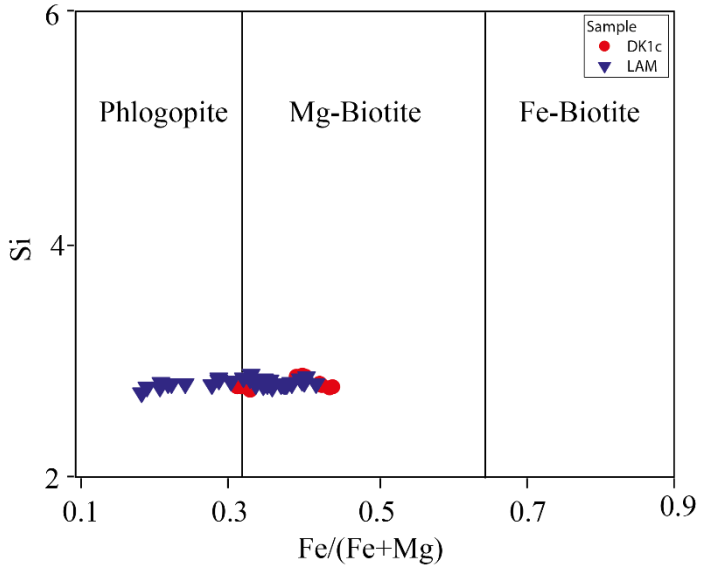


**Figure 10.** The classification of biotites from the dykes of the Sungun deposit [31,34].

### 5.2. Whole Rock Geochemistry

The results of major and trace elements analysis of the Sungun porphyry and of post-mineralization dykes are presented in Tables 4–6. The amount of $SiO_2$ vary from 48.18 to 69.24, and of MgO from 1.47 to 8.27. On the $SiO_2$ versus $Zr/TiO_2$ diagram [35] the sample plot in the andesite, dacite, and rhyodacite fields, which in plutonic terminology are equivalent to diorite, quartz diorite and granodiorite respectively (Figure 11a). Lamprophyre dykes plot in the field of alkaline basalt. The Ta/Yb–Th/Yb diagram [36] shows the shoshonitic nature of the main intrusive suite at Sungun except for the microdiorite samples that have calk-alkaline affinities (Figure 11b).

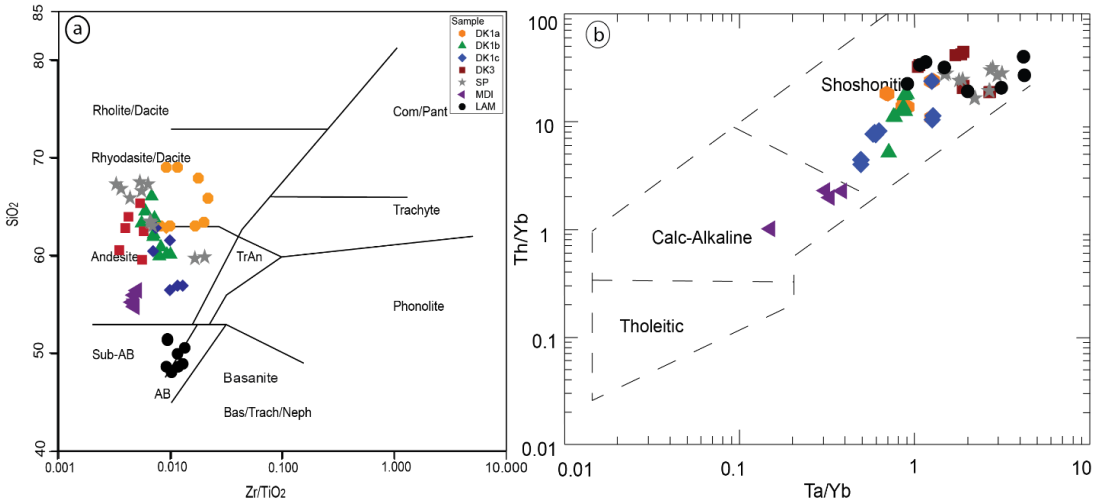


**Figure 11.** General classification of igneous rocks in the Sungun area. (**a**) $SiO_2$ vs. Zr/Ti classification diagram for the Sungun dykes [35]; and (**b**) Ta/Yb-Th/Yb diagram [36].

Sungun lamprophyre dykes span a relatively wide range of $SiO_2$ (48.18–51.54), MgO (7.26–8.34), CaO (1.37–4.96), and $Fe_2O_3$ (3.82–5.65) with Mg numbers of 43–59, similar to potassium-rich lamprophyres. Lamprophyres plot in the calc-alkaline field in the $SiO_2$–CaO–$TiO_2$ diagram (Figure 12a) and compositionally lie within the overlapping field of lamproites and lamprophyres in the $K_2O$–MgO–$Al_2O_3$ diagram (Figure 12b).

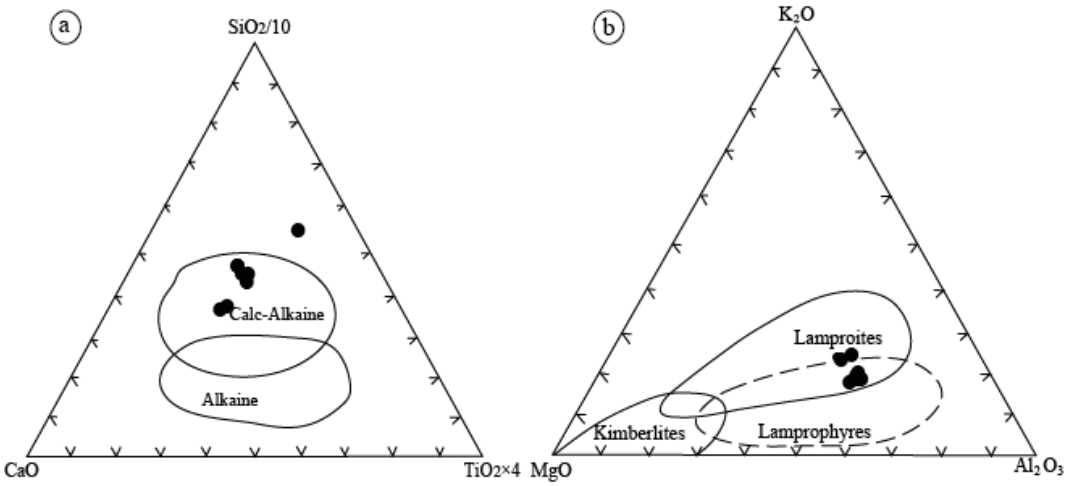


**Figure 12.** (**a**) Ternary plot of $TiO_2$ × 4-$SiO_2$/10-CaO in which Sungun lamprophyres plot in the calc-alkaline field [37] and (**b**) Ternary plot of $K_2O$–MgO–$Al_2O_3$ where the study samples plot across the lamproite/lamprophyre fields [38].

**Table 4.** Major oxide (wt %), trace element (ppm) compositions of dykes (DK1a, DK1b and DK1c) in the Sungun porphyry deposit ((A) analysis by [26]).

| Sample | DK1a-96 | DK1a-553 | DK1a-156 | DK1a-330 | DK1a-A1 | DK1a-A2 | DK1a-A3 | DK1a-A4 | DK1a-A5 | DK1a-A6 | DK1b-A1 |
|---|---|---|---|---|---|---|---|---|---|---|---|
| $SiO_2$ | 67.85 | 62.91 | 65.71 | 63.24 | 62.89 | 62.77 | 62.91 | 62.98 | 69.18 | 69.24 | 62.10 |
| $Al_2O_3$ | 14.12 | 14.07 | 14.17 | 15.45 | 15.01 | 14.96 | 14.86 | 14.93 | 15.58 | 15.55 | 15.06 |
| CaO | 4.09 | 5.71 | 4.55 | 5.12 | 3.44 | 3.47 | 2.26 | 2.29 | 0.36 | 0.39 | 4.12 |
| $Fe_2O_3$ | 2.02 | 2.28 | 1.61 | 1.91 | 3.82 | 3.78 | 3.81 | 3.91 | 3.65 | 3.48 | 4.26 |
| FeO | 2.02 | 2.79 | 1.74 | 2.16 | 2.53 | 2.49 | 1.83 | 1.89 | 2.56 | 2.49 | 2.61 |
| $K_2O$ | 2.78 | 2.36 | 3.69 | 3.39 | 3.38 | 3.29 | 4.48 | 4.51 | 2.96 | 2.98 | 2.71 |
| MgO | 1.51 | 2.08 | 1.47 | 1.78 | 2.13 | 2.17 | 2.61 | 2.58 | 1.56 | 1.52 | 2.38 |
| MnO | 0.10 | 0.09 | 0.11 | 0.12 | 0.07 | 0.06 | 0.02 | 0.04 | 0.05 | 0.04 | 0.08 |
| $Na_2O$ | 3.69 | 2.67 | 2.34 | 2.49 | 4.18 | 4.12 | 4.06 | 4.02 | 3.41 | 3.49 | 4.12 |
| $P_2O_5$ | 0.28 | 0.19 | 0.18 | 0.17 | 0.24 | 0.23 | 0.26 | 0.31 | 0.24 | 0.26 | 0.29 |
| $TiO_2$ | 0.48 | 0.54 | 0.42 | 0.46 | 0.48 | 0.51 | 0.52 | 0.56 | 0.43 | 0.38 | 0.53 |
| LOI | 1.98 | 2.86 | 3.12 | 3.42 | 3.81 | 2.98 | 1.06 | 0.98 | 1.01 | 0.96 | 3.68 |
| Total | 100.92 | 98.55 | 99.11 | 99.71 | 101.98 | 100.83 | 98.68 | 99 | 100.99 | 100.78 | 101.94 |
| Ag | 0.03 | 0.05 | 0.04 | 0.06 | 0.11 | 0.13 | 0.28 | 0.31 | 0.07 | 0.08 | 0.10 |
| As | 11.30 | 10.80 | 11.70 | 12.20 | | | | | | | |
| Au | 0.02 | 0.02 | 0.02 | 0.03 | | | | | | | |
| Ba | 810.00 | 780.00 | 1120.00 | 1080.00 | 1028.00 | 1036.00 | 1241.00 | 1248.00 | 471.00 | 468.00 | 854.00 |
| Be | 1.55 | 1.49 | 1.58 | 1.61 | | | | | | | |
| Bi | 0.08 | 0.06 | 0.09 | 0.11 | 0.21 | 0.23 | 4.10 | 4.20 | 0.20 | 0.30 | 0.10 |
| Cd | 0.02 | 0.03 | 0.01 | 0.04 | 0.08 | 0.09 | 0.16 | 0.18 | 0.21 | 0.19 | 0.07 |
| Ce | 57.00 | 52.00 | 61.40 | 55.00 | 53.20 | 53.70 | 71.80 | 71.20 | 68.20 | 68.40 | 62.40 |
| Co | 8.40 | 9.10 | 9.70 | 8.60 | 10.60 | 10.90 | 14.60 | 14.30 | 8.60 | 8.90 | 12.80 |
| Cr | 10.00 | 12.00 | 17.00 | 16.00 | 26.00 | 27.00 | 41.00 | 43.00 | 24.00 | 23.00 | 41.00 |
| Cs | 1.79 | 1.68 | 1.77 | 1.81 | 1.30 | 1.20 | 2.10 | 2.20 | 3.70 | 3.90 | 1.70 |
| Cu | 31.70 | 32.60 | 35.70 | 28.20 | 81.70 | 83.00 | 951.00 | 942.00 | 3906.00 | 38.80 | 151.00 |
| Dy | 2.03 | 2.01 | 2.06 | 2.04 | 1.86 | 1.85 | 1.92 | 1.91 | 2.03 | 2.01 | 2.38 |
| Er | 1.04 | 1.05 | 1.04 | 1.06 | 1.09 | 1.12 | 1.01 | 1.03 | 1.12 | 1.14 | 1.36 |
| Eu | 0.85 | 0.88 | 0.82 | 0.86 | 0.94 | 0.96 | 1.44 | 1.47 | 1.03 | 1.07 | 1.22 |
| Ga | 17.15 | 17.12 | 16.91 | 17.36 | 15.30 | 15.50 | 16.70 | 16.40 | 16.10 | 16.30 | 16.40 |
| Gd | 2.54 | 2.53 | 2.51 | 2.57 | 2.61 | 2.63 | 3.14 | 3.16 | 3.08 | 3.11 | 3.26 |
| Ge | 0.25 | 0.21 | 0.26 | 0.29 | | | | | | | |
| Hf | 2.20 | 2.30 | 2.10 | 2.50 | 1.37 | 1.39 | 1.12 | 1.11 | 1.36 | 1.34 | 1.31 |
| Ho | 0.39 | 0.36 | 0.39 | 0.39 | 0.41 | 0.43 | 0.35 | 0.37 | 0.41 | 0.43 | 0.53 |

**Table 4.** *Cont.*

| Sample | DK1a-96 | DK1a-553 | DK1a-156 | DK1a-330 | DK1a-A1 | DK1a-A2 | DK1a-A3 | DK1a-A4 | DK1a-A5 | DK1a-A6 | DK1b-A1 |
|---|---|---|---|---|---|---|---|---|---|---|---|
| In | 0.02 | 0.02 | 0.02 | 0.02 | | | | | | | |
| La | 31.90 | 29.70 | 32.60 | 28.70 | 29.80 | 30.10 | 40.30 | 40.50 | 39.60 | 39.80 | 37.10 |
| Li | 8.50 | 8.20 | 7.80 | 8.30 | | | | | | | |
| Lu | 0.16 | 0.17 | 0.16 | 0.15 | 0.18 | 0.16 | 0.38 | 0.41 | 0.17 | 0.18 | 0.21 |
| Mo | 2.77 | 2.61 | 2.88 | 2.77 | 3.30 | 3.50 | 3.50 | 3.60 | 2.30 | 2.50 | 1.20 |
| Nb | 13.90 | 13.20 | 12.80 | 14.10 | 10.80 | 10.90 | 13.70 | 13.50 | 6.70 | 6.60 | 12.40 |
| Nd | 20.70 | 20.20 | 20.80 | 20.70 | 19.70 | 19.90 | 29.30 | 29.50 | 26.60 | 26.80 | 24.80 |
| Ni | 10.90 | 11.70 | 12.20 | 10.80 | 21.00 | 22.00 | 31.00 | 32.00 | 22.00 | 24.00 | 27.00 |
| Pb | 19.20 | 20.70 | 18.40 | 19.20 | 19.90 | 19.70 | 14.30 | 14.60 | 41.10 | 40.90 | 17.30 |
| Pr | 5.66 | 5.59 | 5.61 | 5.63 | 5.71 | 5.73 | 8.05 | 8.07 | 7.53 | 7.55 | 6.92 |
| Rb | 75.00 | 79.10 | 72.60 | 81.20 | 67.50 | 67.60 | 99.30 | 99.40 | 122.10 | 122.30 | 56.70 |
| Re | 0.00 | 0.00 | 0.00 | 0.00 | | | | | | | |
| S | 5200.00 | 6100.00 | 5700.00 | 6210.00 | | | | | | | |
| Sb | 1.07 | 1.02 | 1.12 | 1.09 | | | | | | | |
| Se | 5.80 | 5.40 | 5.60 | 5.90 | | | | | | | |
| Sm | 3.22 | 3.21 | 3.24 | 3.29 | 3.08 | 3.09 | 4.18 | 4.21 | 4.03 | 4.05 | 3.78 |
| Sn | 0.70 | 0.60 | 0.70 | 0.80 | 0.90 | 0.70 | 1.40 | 1.60 | 0.80 | 0.90 | 1.10 |
| Sr | 598.00 | 612.00 | 589.00 | 608.00 | 607.00 | 604.00 | 691.00 | 694.00 | 188.00 | 191.00 | 845.00 |
| Ta | 0.87 | 0.88 | 0.82 | 0.85 | 1.36 | 1.38 | 1.18 | 1.16 | 0.68 | 0.71 | 0.98 |
| Tb | 0.33 | 0.32 | 0.31 | 0.35 | 0.39 | 0.37 | 0.41 | 0.44 | 0.41 | 0.43 | 0.46 |
| Te | 0.07 | 0.08 | 0.06 | 0.08 | | | | | | | |
| Th | 13.10 | 12.90 | 13.60 | 13.50 | 11.70 | 11.90 | 21.70 | 21.90 | 17.70 | 17.90 | 14.10 |
| Tm | 0.15 | 0.13 | 0.15 | 0.16 | | | | | | | |
| U | 3.70 | 3.40 | 3.50 | 3.90 | 5.61 | 5.58 | 11.61 | 11.58 | 6.82 | 6.84 | 5.09 |
| V | 62.00 | 69.00 | 59.00 | 64.00 | 77.00 | 78.00 | 66.00 | 67.00 | 59.00 | 58.00 | 81.00 |
| W | 3.90 | 3.20 | 3.80 | 3.10 | 3.10 | 3.30 | 3.60 | 3.80 | 1.40 | 1.70 | 2.20 |
| Y | 9.50 | 9.70 | 9.30 | 9.60 | 10.40 | 10.60 | 9.50 | 9.60 | 10.10 | 10.30 | 13.40 |
| Yb | 0.99 | 0.98 | 0.97 | 1.02 | 1.12 | 1.13 | 0.94 | 0.96 | 1.01 | 1.03 | 1.32 |
| Zn | 77.00 | 71.00 | 78.00 | 81.00 | 54.60 | 54.30 | 32.80 | 32.60 | 158.10 | 158.30 | 52.60 |
| Zr | 81.60 | 88.20 | 89.10 | 90.20 | 43.00 | 42.00 | 34.00 | 36.00 | 42.00 | 44.00 | 38.00 |

**Table 4.** *Cont.*

| Sample | DK1b-A2 | DK1b-A3 | DK1b-A4 | DK1b-A5 | DK1b-A6 | DK1b-128 | DK1b-593 | DK1b-615 | DK1b-200 | DK1c-558 | DK1c-351 |
|---|---|---|---|---|---|---|---|---|---|---|---|
| $SiO_2$ | 61.98 | 60.08 | 59.98 | 60.71 | 60.08 | 63.81 | 64.61 | 66.20 | 63.19 | 60.12 | 62.19 |
| $Al_2O_3$ | 15.01 | 16.12 | 16.18 | 14.58 | 14.51 | 14.33 | 16.05 | 14.70 | 14.82 | 15.29 | 14.66 |
| CaO | 4.08 | 4.61 | 4.69 | 5.14 | 5.21 | 4.49 | 2.88 | 3.06 | 3.56 | 5.25 | 5.75 |
| $Fe_2O_3$ | 4.29 | 5.51 | 5.58 | 3.41 | 3.38 | 2.36 | 2.70 | 2.43 | 3.31 | 2.84 | 2.57 |
| FeO | 2.58 | 2.61 | 2.72 | 2.08 | 2.12 | 2.36 | 2.98 | 2.70 | 3.34 | 2.90 | 2.96 |
| $K_2O$ | 2.68 | 2.38 | 2.44 | 3.11 | 3.24 | 2.45 | 2.97 | 2.41 | 2.54 | 2.37 | 2.46 |
| MgO | 2.42 | 3.08 | 3.17 | 2.18 | 2.27 | 2.27 | 2.86 | 3.07 | 2.96 | 2.72 | 3.36 |
| MnO | 0.07 | 0.11 | 0.09 | 0.07 | 0.06 | 0.09 | 0.08 | 0.07 | 0.13 | 0.08 | 0.13 |
| $Na_2O$ | 4.08 | 4.49 | 4.51 | 4.77 | 4.73 | 4.46 | 2.78 | 2.84 | 3.01 | 4.23 | 2.78 |
| $P_2O_5$ | 0.31 | 0.31 | 0.32 | 0.27 | 0.29 | 0.23 | 0.19 | 0.21 | 0.22 | 0.26 | 0.24 |
| $TiO_2$ | 0.51 | 0.61 | 0.59 | 0.49 | 0.46 | 0.52 | 0.62 | 0.58 | 0.64 | 0.63 | 0.58 |
| LOI | 3.06 | 2.18 | 1.98 | 3.81 | 3.23 | 1.92 | 1.22 | 1.70 | 2.28 | 2.81 | 2.31 |
| Total | 101.07 | 102.09 | 102.25 | 100.62 | 99.58 | 99.29 | 99.94 | 99.97 | 100 | 99.5 | 99.99 |
| Ag | 0.12 | 0.13 | 0.14 | 0.10 | 0.11 | 0.03 | 0.03 | 0.02 | 0.05 | 0.03 | 0.03 |
| As | | | | | | 1.70 | 1.60 | 1.20 | 1.80 | 1.10 | 1.30 |
| Au | | | | | | 0.01 | 0.00 | 0.01 | 0.00 | 0.00 | 0.00 |
| Ba | 856.00 | 724.00 | 726.00 | 857.00 | 859.00 | 860.00 | 921.00 | 1070.00 | 895.00 | 770.00 | 790.00 |
| Be | | | | | | 1.31 | 1.29 | 1.33 | 1.38 | 1.09 | 1.09 |
| Bi | 0.10 | 0.20 | 0.10 | 0.30 | 0.20 | 0.11 | 0.12 | 0.14 | 0.17 | 0.13 | 0.15 |
| Cd | 0.09 | 0.08 | 0.09 | 0.09 | 0.11 | 0.03 | 0.02 | 0.06 | 0.02 | 0.03 | 0.04 |
| Ce | 62.60 | 45.80 | 45.50 | 70.80 | 71.10 | 50.30 | 49.80 | 51.20 | 54.00 | 49.00 | 44.00 |
| Co | 12.90 | 16.20 | 16.50 | 9.10 | 9.30 | 10.90 | 10.70 | 9.80 | 11.20 | 13.50 | 12.80 |
| Cr | 40.00 | 27.00 | 28.00 | 31.00 | 33.00 | 31.00 | 33.00 | 28.00 | 39.00 | 27.00 | 26.00 |
| Cs | 1.60 | 0.60 | 0.70 | 1.10 | 1.30 | 0.60 | 0.62 | 0.71 | 0.62 | 0.66 | 0.61 |
| Cu | 153.00 | 144.00 | 143.00 | 127.00 | 128.00 | 68.00 | 58.10 | 62.60 | 48.10 | 49.60 | 45.20 |
| Dy | 2.41 | 2.46 | 2.43 | 2.27 | 2.29 | 2.12 | 2.16 | 2.13 | 2.11 | 2.56 | 2.48 |
| Er | 1.38 | 1.39 | 1.41 | 1.22 | 1.23 | 1.09 | 1.09 | 1.08 | 1.07 | 1.39 | 1.38 |
| Eu | 1.24 | 1.07 | 1.08 | 1.11 | 1.09 | 0.96 | 0.97 | 0.93 | 0.95 | 1.09 | 1.08 |
| Ga | 16.70 | 17.50 | 17.30 | 16.60 | 16.30 | 17.30 | 17.14 | 17.37 | 16.91 | 17.35 | 17.14 |
| Gd | 3.28 | 3.12 | 3.09 | 3.09 | 3.13 | 2.68 | 2.62 | 2.70 | 2.66 | 3.25 | 3.21 |
| Ge | | | | | | 0.20 | 0.21 | 0.22 | 0.19 | 0.24 | 0.25 |

**Table 4.** *Cont.*

| Sample | DK1b-A2 | DK1b-A3 | DK1b-A4 | DK1b-A5 | DK1b-A6 | DK1b-128 | DK1b-593 | DK1b-615 | DK1b-200 | DK1c-558 | DK1c-351 |
|---|---|---|---|---|---|---|---|---|---|---|---|
| Hf | 1.33 | 1.92 | 1.95 | 1.46 | 1.49 | 1.30 | 1.20 | 1.30 | 1.10 | 1.70 | 1.60 |
| Ho | 0.52 | 0.52 | 0.51 | 0.46 | 0.48 | 0.40 | 0.42 | 0.47 | 0.44 | 0.51 | 0.53 |
| In | | | | | | 0.04 | 0.03 | 0.04 | 0.03 | 0.04 | 0.03 |
| La | 37.00 | 24.90 | 24.70 | 42.30 | 42.50 | 28.30 | 28.60 | 27.20 | 29.70 | 28.20 | 28.30 |
| Li | | | | | | 10.00 | 10.30 | 9.80 | 9.30 | 9.70 | 9.50 |
| Lu | 0.23 | 0.21 | 0.22 | 0.18 | 0.16 | 0.15 | 0.16 | 0.18 | 0.14 | 0.20 | 0.18 |
| Mo | 1.40 | 2.80 | 2.90 | 4.20 | 4.30 | 2.72 | 2.69 | 2.78 | 2.81 | 2.47 | 2.46 |
| Nb | 12.20 | 11.60 | 11.70 | 11.20 | 11.40 | 12.70 | 12.20 | 11.80 | 12.40 | 11.00 | 11.90 |
| Nd | 24.90 | 19.80 | 20.10 | 26.60 | 26.80 | 19.70 | 19.30 | 19.60 | 19.90 | 20.70 | 20.60 |
| Ni | 25.00 | 22.00 | 23.00 | 24.00 | 25.00 | 20.80 | 21.20 | 20.20 | 19.80 | 20.60 | 21.20 |
| Pb | 17.40 | 14.10 | 14.30 | 9.60 | 9.70 | 21.70 | 22.20 | 23.70 | 20.60 | 10.00 | 10.60 |
| Pr | 6.96 | 5.19 | 5.15 | 7.61 | 7.63 | 5.29 | 5.31 | 5.27 | 5.24 | 5.29 | 5.31 |
| Rb | 56.50 | 37.10 | 37.20 | 65.50 | 65.20 | 57.90 | 59.40 | 56.20 | 57.40 | 47.40 | 48.60 |
| Re | | | | | | 0.00 | 0.00 | 0.00 | 0.00 | 0.00 | 0.00 |
| S | | | | | | 3100.00 | 3260.00 | 3310.00 | 3000.00 | 2000.00 | 2100.00 |
| Sb | | | | | | 0.81 | 0.84 | 0.91 | 0.77 | 0.55 | 0.59 |
| Se | | | | | | 8.00 | 8.20 | 8.60 | 7.80 | 10.70 | 10.20 |
| Sm | 3.81 | 3.31 | 3.34 | 3.76 | 3.74 | 3.17 | 3.18 | 3.21 | 3.14 | 3.70 | 3.71 |
| Sn | 0.90 | 1.00 | 0.90 | 0.80 | 0.90 | 0.80 | 0.60 | 0.70 | 0.80 | 0.90 | 0.90 |
| Sr | 847.00 | 805.00 | 807.00 | 667.00 | 664.00 | 725.00 | 736.00 | 742.00 | 718.00 | 650.00 | 662.00 |
| Ta | 0.99 | 0.91 | 0.93 | 0.98 | 0.99 | 0.85 | 0.86 | 0.89 | 0.84 | 0.73 | 0.72 |
| Tb | 0.44 | 0.43 | 0.47 | 0.43 | 0.45 | 0.35 | 0.32 | 0.35 | 0.37 | 0.43 | 0.44 |
| Te | | | | | | 0.05 | 0.05 | 0.07 | 0.05 | 0.05 | 0.06 |
| Th | 13.90 | 6.50 | 6.60 | 19.20 | 19.40 | 12.80 | 12.60 | 12.40 | 12.90 | 9.60 | 9.40 |
| Tm | | | | | | 0.15 | 0.14 | 0.15 | 0.17 | 0.19 | 0.18 |
| U | 5.07 | 3.21 | 5.24 | 4.96 | 4.95 | 3.80 | 3.80 | 4.10 | 3.20 | 2.90 | 2.60 |
| V | 82.00 | 112.00 | 111.00 | 61.00 | 59.00 | 86.00 | 82.00 | 91.00 | 86.00 | 102.00 | 104.00 |
| W | 1.90 | 1.20 | 1.30 | 13.20 | 13.40 | 2.50 | 2.60 | 2.20 | 2.10 | 1.10 | 1.30 |
| Y | 13.20 | 13.10 | 12.90 | 12.50 | 12.30 | 9.80 | 9.40 | 9.30 | 8.90 | 13.10 | 13.20 |
| Yb | 1.31 | 1.31 | 1.33 | 1.14 | 1.12 | 1.02 | 1.01 | 1.03 | 0.99 | 1.26 | 1.27 |
| Zn | 52.80 | 70.90 | 70.70 | 43.10 | 43.30 | 64.00 | 61.00 | 58.00 | 62.00 | 51.00 | 48.00 |
| Zr | 36.00 | 58.00 | 60.00 | 39.00 | 37.00 | 37.40 | 36.40 | 39.10 | 35.20 | 50.50 | 51.70 |

**Table 5.** Major oxide (wt %), trace element (ppm) compositions of dykes (DK1c, DK3 and MDI) in the Sungun porphyry deposit ((A) analysis by [26]).

| Sample | DK1c-417 | DK1c-145 | DK1c-A1 | DK1c-A2 | DK1c-A3 | DK1c-A4 | DK1c-A5 | DK1c-A6 | DK3–190 | DK3-103 | DK3-25 |
|---|---|---|---|---|---|---|---|---|---|---|---|
| $SiO_2$ | 61.51 | 60.53 | 62.88 | 62.81 | 62.81 | 56.45 | 56.81 | 56.88 | 65.38 | 63.72 | 60.49 |
| $Al_2O_3$ | 14.89 | 14.62 | 15.01 | 14.89 | 14.81 | 16.31 | 15.13 | 15.21 | 12.62 | 14.21 | 13.70 |
| CaO | 5.82 | 6.92 | 3.44 | 3.41 | 2.26 | 6.12 | 6.01 | 5.98 | 6.27 | 5.86 | 7.17 |
| $Fe_2O_3$ | 2.95 | 2.96 | 3.81 | 3.78 | 3.81 | 6.07 | 6.12 | 6.08 | 1.83 | 2.28 | 2.92 |
| FeO | 3.46 | 3.69 | 2.61 | 2.58 | 1.81 | 3.14 | 2.71 | 2.68 | 1.83 | 2.78 | 3.43 |
| $K_2O$ | 2.99 | 2.08 | 3.31 | 3.28 | 4.48 | 1.93 | 2.03 | 2.01 | 0.16 | 2.04 | 1.92 |
| MgO | 3.13 | 3.82 | 2.13 | 2.24 | 2.48 | 3.68 | 4.81 | 4.79 | 2.07 | 3.32 | 4.02 |
| MnO | 0.12 | 0.12 | 0.07 | 0.08 | 0.03 | 0.10 | 0.12 | 0.12 | 0.10 | 0.09 | 0.15 |
| $Na_2O$ | 2.38 | 2.61 | 4.21 | 4.18 | 4.10 | 4.10 | 4.05 | 4.08 | 6.47 | 2.65 | 3.46 |
| $P_2O_5$ | 0.21 | 0.23 | 0.26 | 0.28 | 0.29 | 0.41 | 0.33 | 0.34 | 0.22 | 0.21 | 0.25 |
| $TiO_2$ | 0.54 | 0.73 | 0.49 | 0.51 | 0.53 | 0.68 | 0.69 | 0.62 | 0.45 | 0.56 | 0.68 |
| LOI | 2.28 | 2.12 | 3.81 | 3.68 | 1.06 | 2.12 | 2.38 | 2.18 | 2.68 | 1.98 | 2.01 |
| Total | 100.28 | 100.43 | 102.03 | 101.72 | 98.47 | 101.11 | 101.19 | 100.97 | 100.08 | 99.7 | 100.2 |
| Ag | 0.02 | 0.05 | 0.10 | 0.11 | 0.28 | 0.08 | 0.12 | 0.11 | 0.06 | 0.06 | 0.09 |
| As | 1.10 | 1.60 | | | | | | | 5.20 | 5.40 | 4.80 |
| Au | 0.00 | 0.00 | | | | | | | 0.00 | 0.00 | 0.00 |
| Ba | 810.00 | 768.00 | 1032.00 | 1038.00 | 1245.00 | 586.00 | 677.00 | 672.00 | 30.00 | 45.00 | 48.00 |
| Be | 0.98 | 1.12 | | | | | | | 2.08 | 2.18 | 2.02 |
| Bi | 0.18 | 0.19 | 0.20 | 0.30 | 4.10 | 0.01 | 0.13 | 0.12 | 0.36 | 0.39 | 0.41 |
| Cd | 0.06 | 0.02 | 0.09 | 0.11 | 0.14 | 0.07 | 0.09 | 0.08 | 0.06 | 0.05 | 0.04 |
| Ce | 47.60 | 45.90 | 54.80 | 53.90 | 71.80 | 61.60 | 51.70 | 51.40 | 71.40 | 72.20 | 69.60 |
| Co | 13.90 | 14.00 | 10.90 | 11.10 | 14.80 | 19.10 | 23.20 | 23.60 | 4.70 | 4.60 | 4.40 |
| Cr | 31.00 | 28.00 | 27.00 | 28.00 | 41.00 | 34.00 | 122.00 | 121.00 | 50.00 | 52.00 | 48.00 |
| Cs | 0.72 | 0.77 | 1.20 | 1.30 | 2.20 | 0.50 | 0.60 | 0.70 | 0.21 | 0.24 | 0.26 |
| Cu | 43.10 | 39.70 | 83.30 | 84.60 | 943.00 | 57.00 | 101.00 | 107.00 | 48.80 | 46.40 | 41.10 |
| Dy | 2.52 | 2.57 | 1.86 | 1.88 | 1.96 | 3.12 | 3.11 | 3.14 | 1.35 | 1.36 | 1.35 |
| Er | 1.36 | 1.40 | 1.12 | 1.08 | 1.01 | 1.77 | 1.71 | 1.73 | 0.65 | 0.66 | 0.65 |
| Eu | 1.12 | 1.06 | 0.93 | 0.97 | 1.47 | 1.31 | 1.26 | 1.28 | 0.47 | 0.44 | 0.49 |
| Ga | 16.96 | 16.62 | 15.60 | 15.30 | 16.70 | 18.20 | 17.30 | 17.40 | 12.45 | 13.01 | 13.26 |
| Gd | 3.26 | 3.29 | 2.58 | 2.56 | 3.15 | 4.11 | 3.81 | 3.87 | 2.08 | 2.06 | 2.02 |
| Ge | 0.23 | 0.21 | | | | | | | 0.21 | 0.22 | 0.25 |
| Hf | 1.80 | 1.60 | 1.38 | 1.39 | 1.12 | 2.14 | 2.17 | 2.15 | 1.00 | 1.20 | 0.90 |
| Ho | 0.55 | 0.49 | 0.41 | 0.39 | 0.37 | 0.64 | 0.67 | 0.66 | 0.24 | 0.26 | 0.22 |

**Table 5.** *Cont.*

| Sample | DK1c-417 | DK1c-145 | DK1c-A1 | DK1c-A2 | DK1c-A3 | DK1c-A4 | DK1c-A5 | DK1c-A6 | DK3–190 | DK3-103 | DK3-25 |
|---|---|---|---|---|---|---|---|---|---|---|---|
| In | 0.03 | 0.02 | | | | | | | 0.20 | 0.04 | 0.20 |
| La | 29.10 | 27.20 | 29.80 | 30.10 | 40.30 | 34.70 | 28.30 | 28.60 | 40.60 | 41.20 | 39.80 |
| Li | 8.70 | 9.10 | | | | | | | 2.30 | 2.20 | 2.60 |
| Lu | 0.21 | 0.23 | 0.18 | 0.16 | 0.38 | 0.27 | 0.28 | 0.29 | 0.07 | 0.06 | 0.08 |
| Mo | 2.32 | 2.37 | 3.30 | 3.60 | 3.70 | 2.20 | 1.70 | 1.60 | 3.31 | 3.41 | 3.51 |
| Nb | 10.80 | 11.40 | 10.80 | 10.90 | 13.70 | 11.60 | 12.30 | 12.40 | 15.50 | 16.70 | 15.20 |
| Nd | 20.90 | 20.30 | 19.80 | 19.90 | 29.30 | 27.30 | 23.20 | 23.60 | 23.90 | 23.80 | 23.40 |
| Ni | 21.70 | 20.60 | 21.00 | 23.00 | 31.00 | 31.00 | 42.00 | 69.00 | 26.90 | 27.60 | 26.20 |
| Pb | 11.20 | 9.80 | 19.70 | 19.30 | 14.30 | 11.90 | 7.20 | 7.60 | 9.90 | 9.60 | 8.90 |
| Pr | 5.26 | 5.28 | 5.81 | 5.77 | 8.31 | 7.21 | 6.06 | 6.12 | 7.37 | 7.32 | 7.39 |
| Rb | 50.10 | 51.70 | 67.30 | 67.50 | 99.30 | 37.80 | 39.40 | 40.10 | 2.70 | 2.90 | 3.40 |
| Re | 0.00 | 0.00 | | | | | | | 0.01 | 0.01 | 0.01 |
| S | 2400.00 | 1900.00 | | | | | | | 3300.00 | 3460.00 | 3100.00 |
| Sb | 0.48 | 0.52 | | | | | | | 1.92 | 1.69 | 1.88 |
| Se | 11.10 | 10.80 | | | | | | | 6.60 | 6.60 | 6.80 |
| Sm | 3.77 | 3.68 | 3.08 | 3.05 | 4.21 | 4.34 | 4.01 | 4.06 | 3.10 | 3.12 | 3.16 |
| Sn | 0.80 | 0.60 | 0.70 | 0.90 | 1.60 | 0.90 | 0.90 | 1.10 | 0.90 | 0.70 | 0.60 |
| Sr | 626.00 | 672.00 | 605.00 | 604.00 | 698.00 | 867.00 | 771.00 | 781.00 | 316.00 | 321.00 | 334.00 |
| Ta | 0.76 | 0.74 | 1.36 | 1.37 | 1.18 | 0.85 | 0.80 | 0.82 | 0.95 | 0.97 | 0.92 |
| Tb | 0.42 | 0.41 | 0.39 | 0.37 | 0.41 | 0.56 | 0.57 | 0.59 | 0.16 | 0.17 | 0.16 |
| Te | 0.07 | 0.05 | | | | | | | 0.27 | 0.26 | 0.29 |
| Th | 9.80 | 9.20 | 11.90 | 11.10 | 21.90 | 6.80 | 7.10 | 7.20 | 21.80 | 22.10 | 21.80 |
| Tm | 0.17 | 0.15 | | | | | | | 0.08 | 0.09 | 0.08 |
| U | 2.80 | 3.10 | 5.51 | 5.58 | 11.71 | 2.44 | 2.61 | 2.66 | 3.20 | 3.30 | 3.70 |
| V | 98.00 | 105.00 | 77.00 | 74.00 | 65.00 | 122.00 | 132.00 | 136.00 | 62.00 | 63.00 | 69.00 |
| W | 0.90 | 1.40 | 3.40 | 3.30 | 3.80 | 1.00 | 1.20 | 1.10 | 1.40 | 1.30 | 1.10 |
| Y | 13.70 | 13.60 | 10.52 | 10.53 | 9.58 | 16.60 | 17.20 | 17.30 | 6.80 | 6.50 | 6.90 |
| Yb | 1.24 | 1.26 | 1.09 | 1.11 | 0.96 | 1.76 | 1.66 | 1.69 | 0.51 | 0.52 | 0.55 |
| Zn | 54.00 | 42.00 | 54.10 | 54.90 | 32.80 | 89.30 | 80.50 | 81.20 | 24.00 | 21.00 | 23.00 |
| Zr | 53.20 | 50.60 | 43.00 | 44.00 | 39.00 | 69.00 | 78.00 | 81.00 | 24.00 | 23.70 | 22.60 |

**Table 5.** *Cont.*

| Sample | DK3-320 | DK3-A1 | DK3-A2 | DK3-A3 | DK3-A4 | DK3-A5 | DK3-A6 | MDI-416 | MDI-196 | MDI-132 | MDI-146 |
|---|---|---|---|---|---|---|---|---|---|---|---|
| $SiO_2$ | 62.72 | 62.54 | 62.51 | 59.55 | 59.57 | 62.91 | 62.95 | 54.68 | 55.12 | 56.08 | 54.48 |
| $Al_2O_3$ | 13.81 | 15.18 | 15.21 | 14.61 | 14.58 | 14.88 | 14.86 | 16.06 | 16.16 | 15.81 | 16.12 |
| CaO | 6.48 | 2.91 | 2.94 | 5.58 | 5.56 | 4.02 | 4.01 | 10.12 | 9.98 | 9.36 | 9.82 |
| $Fe_2O_3$ | 2.88 | 2.51 | 2.48 | 4.51 | 4.48 | 2.12 | 2.08 | 3.68 | 3.74 | 3.47 | 3.55 |
| FeO | 3.18 | 1.28 | 1.31 | 1.51 | 1.48 | 1.21 | 1.18 | 5.02 | 5.08 | 4.71 | 4.82 |
| $K_2O$ | 2.14 | 7.32 | 7.38 | 3.21 | 3.18 | 2.41 | 2.38 | 2.94 | 2.96 | 2.88 | 2.86 |
| MgO | 3.38 | 2.58 | 2.64 | 3.81 | 3.78 | 2.61 | 2.65 | 3.53 | 3.62 | 3.72 | 3.62 |
| MnO | 0.11 | 0.02 | 0.02 | 0.12 | 0.10 | 0.06 | 0.05 | 0.13 | 0.14 | 0.13 | 0.14 |
| $Na_2O$ | 3.66 | 3.41 | 3.38 | 5.41 | 5.38 | 5.77 | 5.78 | 1.13 | 1.16 | 1.26 | 1.26 |
| $P_2O_5$ | 0.22 | 0.31 | 0.32 | 0.32 | 0.34 | 0.31 | 0.31 | 0.27 | 0.26 | 0.27 | 0.28 |
| $TiO_2$ | 0.62 | 0.58 | 0.59 | 0.57 | 0.58 | 0.51 | 0.53 | 0.88 | 0.91 | 0.82 | 0.82 |
| LOI | 1.36 | 0.51 | 0.48 | 1.68 | 1.65 | 3.13 | 3.21 | 2.36 | 1.98 | 2.06 | 2.12 |
| Total | 100.56 | 99.15 | 99.26 | 100.88 | 100.68 | 99.94 | 99.99 | 100.8 | 101.11 | 100.57 | 99.89 |
| Ag | 0.06 | 0.25 | 0.23 | 0.22 | 0.21 | 0.13 | 0.11 | 0.07 | 0.08 | 0.09 | 0.06 |
| As | 4.60 | | | | | | | 2.70 | 2.90 | 2.61 | 3.10 |
| Au | 0.00 | | | | | | | 0.01 | 0.00 | 0.00 | 0.00 |
| Ba | 72.00 | 1128.00 | 1119.00 | 877.00 | 881.00 | 698.00 | 691.00 | 1310.00 | 1360.00 | 998.00 | 1240.00 |
| Be | 1.98 | | | | | | | 0.94 | 0.96 | 0.98 | 1.02 |
| Bi | 0.34 | 1.10 | 1.00 | 60.20 | 61.80 | 1.20 | 1.30 | 0.19 | 0.18 | 0.19 | 0.21 |
| Cd | 0.02 | 0.06 | 0.06 | 0.14 | 0.15 | 0.07 | 0.08 | 0.06 | 0.07 | 0.04 | 0.06 |
| Ce | 70.00 | 41.60 | 41.30 | 51.70 | 51.40 | 106.00 | 103.80 | 24.30 | 25.60 | 29.70 | 24.20 |
| Co | 5.10 | 5.30 | 5.40 | 10.70 | 10.80 | 5.10 | 5.30 | 27.90 | 29.10 | 28.60 | 27.00 |
| Cr | 54.00 | 52.00 | 53.00 | 88.00 | 91.00 | 54.00 | 57.00 | 4.00 | 6.00 | 7.00 | 3.00 |
| Cs | 0.19 | 0.50 | 0.60 | 0.20 | 0.30 | 0.80 | 0.80 | 6.85 | 6.94 | 6.15 | 5.91 |
| Cu | 38.70 | 470.00 | 477.00 | 39.60 | 38.80 | 89.10 | 87.40 | 79.00 | 75.10 | 41.20 | 38.20 |
| Dy | 1.37 | 1.66 | 1.64 | 1.53 | 1.57 | 1.88 | 1.91 | 3.75 | 3.72 | 3.77 | 3.71 |
| Er | 0.67 | 0.85 | 0.83 | 0.81 | 0.79 | 1.01 | 1.03 | 1.96 | 1.94 | 1.92 | 1.97 |
| Eu | 0.51 | 0.74 | 0.75 | 0.86 | 0.83 | 1.21 | 1.26 | 1.20 | 1.18 | 1.22 | 1.19 |
| Ga | 12.98 | 15.70 | 15.80 | 14.50 | 14.90 | 16.70 | 16.90 | 16.40 | 17.10 | 16.12 | 17.18 |
| Gd | 2.11 | 2.35 | 2.37 | 2.32 | 2.34 | 3.32 | 3.29 | 4.01 | 4.06 | 4.02 | 4.07 |
| Ge | 0.19 | | | | | | | 0.21 | 0.22 | 0.19 | 0.18 |
| Hf | 4.30 | 1.32 | 1.34 | 1.17 | 1.19 | 1.01 | 1.03 | 1.50 | 1.60 | 1.90 | 1.80 |

**Table 5.** *Cont.*

| Sample | DK3-320 | DK3-A1 | DK3-A2 | DK3-A3 | DK3-A4 | DK3-A5 | DK3-A6 | MDI-416 | MDI-196 | MDI-132 | MDI-146 |
|---|---|---|---|---|---|---|---|---|---|---|---|
| Ho | 0.27 | 0.33 | 0.35 | 0.30 | 0.32 | 0.37 | 0.36 | 0.73 | 0.77 | 0.71 | 0.74 |
| In | 0.20 | | | | | | | 0.05 | 0.06 | 0.05 | 0.06 |
| La | 41.60 | 20.10 | 20.30 | 27.70 | 27.90 | 67.80 | 67.70 | 11.10 | 10.80 | 11.20 | 10.60 |
| Li | 2.40 | | | | | | | 16.30 | 16.70 | 16.20 | 16.90 |
| Lu | 0.07 | 0.16 | 0.14 | 0.11 | 0.09 | 0.15 | 0.13 | 0.30 | 0.31 | 0.33 | 0.29 |
| Mo | 3.44 | 1.20 | 1.40 | 2.10 | 2.30 | 1.20 | 1.10 | 0.77 | 0.78 | 0.79 | 0.81 |
| Nb | 16.10 | 18.40 | 18.20 | 20.50 | 20.70 | 11.90 | 12.10 | 5.10 | 5.20 | 5.80 | 4.60 |
| Nd | 23.10 | 18.80 | 18.90 | 20.70 | 20.50 | 34.80 | 34.60 | 15.00 | 15.60 | 14.90 | 15.40 |
| Ni | 25.70 | 41.00 | 44.00 | 51.00 | 53.00 | 38.00 | 36.00 | 3.50 | 3.20 | 3.40 | 4.10 |
| Pb | 9.40 | 18.10 | 18.30 | 11.40 | 11.60 | 16.70 | 16.40 | 14.80 | 13.20 | 14.10 | 13.60 |
| Pr | 7.31 | 4.81 | 4.81 | 5.89 | 5.93 | 10.71 | 10.78 | 3.27 | 3.29 | 3.24 | 3.30 |
| Rb | 4.20 | 67.80 | 68.10 | 18.90 | 18.20 | 46.00 | 47.00 | 97.60 | 99.20 | 91.60 | 89.40 |
| Re | 0.01 | | | | | | | 0.00 | 0.00 | 0.00 | 0.00 |
| S | 3400.00 | | | | | | | 1800.00 | 1600.00 | 1600.00 | 1460.00 |
| Sb | 1.96 | | | | | | | 0.98 | 0.92 | 0.91 | 0.86 |
| Se | 6.20 | | | | | | | 13.10 | 13.60 | 12.80 | 12.40 |
| Sm | 3.08 | 2.85 | 2.87 | 2.98 | 3.01 | 4.32 | 4.28 | 3.67 | 3.64 | 3.66 | 3.61 |
| Sn | 0.70 | 4.60 | 4.40 | 1.20 | 1.10 | 0.90 | 0.70 | 0.80 | 0.90 | 0.80 | 0.60 |
| Sr | 298.00 | 288.00 | 291.00 | 354.00 | 355.00 | 707.00 | 709.00 | 234.00 | 226.00 | 237.00 | 216.00 |
| Ta | 0.96 | 1.93 | 1.94 | 1.29 | 1.31 | 0.94 | 0.95 | 0.27 | 0.26 | 0.27 | 0.31 |
| Tb | 0.19 | 0.34 | 0.35 | 0.32 | 0.30 | 0.43 | 0.45 | 0.57 | 0.52 | 0.56 | 0.58 |
| Te | 0.24 | | | | | | | 0.05 | 0.04 | 0.05 | 0.06 |
| Th | 21.40 | 13.20 | 13.30 | 14.20 | 14.00 | 28.90 | 28.70 | 1.80 | 1.90 | 1.60 | 1.80 |
| Tm | 0.09 | | | | | | | 0.30 | 0.31 | 0.33 | 0.29 |
| U | 2.90 | 4.36 | 4.34 | 8.08 | 8.05 | 9.36 | 9.41 | 0.50 | 0.50 | 0.70 | 0.60 |
| V | 62.00 | 84.00 | 85.00 | 89.00 | 90.00 | 63.00 | 66.00 | 176.00 | 171.00 | 168.00 | 171.00 |
| W | 1.60 | 3.60 | 3.50 | 1.70 | 1.80 | 7.20 | 7.80 | 1.10 | 1.20 | 0.90 | 1.20 |
| Y | 6.60 | 7.99 | 8.01 | 6.96 | 6.99 | 10.51 | 10.48 | 18.80 | 18.20 | 18.60 | 17.90 |
| Yb | 0.53 | 0.73 | 0.74 | 0.69 | 0.71 | 0.90 | 0.93 | 1.84 | 0.86 | 0.84 | 0.82 |
| Zn | 27.00 | 27.90 | 27.70 | 47.50 | 47.60 | 42.90 | 43.10 | 122.00 | 126.00 | 118.00 | 116.00 |
| Zr | 25.00 | 34.00 | 35.00 | 31.00 | 33.00 | 32.00 | 36.00 | 42.40 | 43.40 | 42.10 | 42.60 |

**Table 6.** Major oxide (wt %), trace element (ppm) compositions of lamprophyre dykes (LAM) and Sungun porphyry stock (SP) in the Sungun deposit ((A) analysis by [26]).

| Sample | SPA1 | SPA2 | SPA3 | SPA4 | SPA5 | SPA6 | SPA7 | SPA8 | SPA9 | SPA10 | SPA11 | SPA12 |
|---|---|---|---|---|---|---|---|---|---|---|---|---|
| $SiO_2$ | 65.88 | 67.15 | 67.08 | 59.71 | 59.62 | 66.03 | 67.01 | 66.98 | 63.31 | 63.34 | 62.41 | 62.36 |
| $Al_2O_3$ | 15.17 | 14.48 | 14.51 | 14.01 | 14.02 | 15.18 | 14.72 | 14.74 | 13.42 | 13.41 | 14.86 | 14.91 |
| CaO | 2.43 | 0.32 | 0.31 | 6.02 | 5.96 | 2.48 | 0.48 | 0.49 | 3.08 | 3.06 | 0.48 | 0.47 |
| $Fe_2O_3$ | 2.8 | 2.41 | 2.36 | 3.38 | 3.32 | 2.72 | 3.58 | 3.61 | 2.71 | 2.78 | 6.08 | 6.02 |
| FeO | 1.68 | 1.88 | 1.85 | 2.05 | 2.06 | 2.08 | 2.61 | 2.58 | 2.42 | 2.86 | 0.95 | 0.94 |
| $K_2O$ | 5.06 | 9.41 | 9.13 | 6.38 | 6.32 | 5.01 | 6.32 | 6.28 | 7.68 | 7.71 | 6.31 | 6.28 |
| MgO | 1.51 | 1.58 | 1.55 | 2.32 | 2.34 | 1.58 | 2.68 | 2.65 | 2.08 | 2.12 | 2.88 | 2.91 |
| MnO | 0.02 | 0.01 | 0.01 | 0.06 | 0.05 | 0.02 | 0.01 | 0.01 | 0.01 | 0.01 | 0.01 | 0.01 |
| $Na_2O$ | 4.2 | 0.71 | 0.68 | 2.62 | 2.58 | 4.06 | 0.35 | 0.36 | 0.62 | 0.65 | 0.19 | 0.18 |
| $P_2O_5$ | 0.27 | 0.23 | 0.25 | 0.41 | 0.42 | 0.21 | 0.32 | 0.33 | 0.31 | 0.33 | 0.3 | 0.31 |
| $TiO_2$ | 0.41 | 0.42 | 0.41 | 0.58 | 0.55 | 0.38 | 0.51 | 0.51 | 0.48 | 0.51 | 0.52 | 0.51 |
| LOI | 0.32 | 0.01 | 0.02 | 2.98 | 2.81 | 0.32 | 0.01 | 0.02 | 2.58 | 2.31 | 0.01 | 0.02 |
| Total | 99.75 | 98.61 | 98.16 | 100.52 | 100.05 | 100.07 | 98.6 | 98.56 | 98.7 | 99.09 | 95 | 94.92 |
| Ag | 0.25 | 0.89 | 0.92 | 0.26 | 0.27 | 0.28 | 0.56 | 0.61 | 0.96 | 0.98 | 0.18 | 0.19 |
| As | | | | | | | | | | | | |
| Au | | | | | | | | | | | | |
| Ba | 1870 | 1671 | 1681 | 1117 | 1127 | 1886 | 1281 | 1282 | 1427 | 1431 | 1502 | 1517 |
| Be | | | | | | | | | | | | |
| Bi | 1 | 0.7 | 0.6 | 0.4 | 0.5 | 1.2 | 0.8 | 0.8 | 0.8 | 0.6 | 0.9 | 0.9 |
| Cd | 0.15 | 0.27 | 0.31 | 0.09 | 0.12 | 0.17 | 0.31 | 0.42 | 0.32 | 0.41 | 0.12 | 0.15 |
| Ce | 51.8 | 122 | 124 | 69.2 | 70.1 | 52.6 | 70.6 | 70.8 | 28.9 | 29.1 | 31.7 | 32.2 |
| Co | 8.3 | 2.3 | 2.5 | 11.2 | 11.4 | 8.8 | 7.1 | 7.3 | 9.4 | 9.6 | 29.4 | 29.7 |
| Cr | 38 | 35 | 37 | 61 | 64 | 41 | 61 | 63 | 52 | 54 | 79 | 81 |
| Cs | 1.3 | 1.6 | 1.8 | 1.1 | 1.3 | 1.2 | 3.3 | 3.4 | 3.7 | 3.5 | 0.9 | 1.1 |
| Cu | 578.6 | 11120 | 11210 | 197.6 | 200.5 | 580.9 | 6033 | 6037 | 5596 | 5592 | 1580 | 1591 |
| Dy | 1.56 | 1.06 | 1.07 | 1.94 | 1.96 | 1.57 | 1.43 | 1.45 | 1.36 | 1.34 | 0.96 | 0.94 |
| Er | 0.87 | 0.48 | 0.46 | 1.03 | 1.06 | 0.88 | 0.66 | 0.67 | 0.77 | 0.78 | 0.48 | 0.44 |
| Eu | 1.06 | 1.04 | 1.07 | 1.36 | 1.35 | 1.07 | 1.12 | 1.08 | 0.66 | 0.69 | 0.64 | 0.71 |
| Ga | 15 | 14 | 17 | 16 | 16 | 17 | 15.8 | 16.1 | 15.3 | 15.4 | 15.8 | 15.9 |
| Gd | 2.36 | 2.14 | 2.17 | 3.26 | 3.25 | 2.41 | 2.66 | 2.64 | 1.95 | 1.93 | 1.42 | 1.46 |
| Hf | 1.38 | 0.99 | 1.02 | 2.96 | 2.98 | 1.41 | 0.46 | 0.47 | 0.94 | 0.96 | 1.17 | 1.18 |
| Ho | 0.35 | 0.22 | 0.23 | 0.41 | 0.38 | 0.37 | 0.27 | 0.29 | 0.29 | 0.31 | 0.18 | 0.17 |

**Table 6.** *Cont.*

| Sample | SPA1 | SPA2 | SPA3 | SPA4 | SPA5 | SPA6 | SPA7 | SPA8 | SPA9 | SPA10 | SPA11 | SPA12 |
|---|---|---|---|---|---|---|---|---|---|---|---|---|
| La | 27.8 | 132 | 134 | 36.7 | 37.1 | 28.1 | 39.6 | 39.5 | 15.1 | 15.7 | 16.7 | 16.9 |
| Lu | 0.65 | 0.29 | 0.31 | 0.22 | 0.24 | 0.66 | 0.11 | 0.13 | 0.12 | 0.12 | 0.1 | 0.11 |
| Mo | 1.9 | 12.8 | 13.1 | 2.6 | 2.9 | 2.2 | 253 | 256 | 23.7 | 24.1 | 2.9 | 3.2 |
| Nb | 18.2 | 5.7 | 5.8 | 20.8 | 21.1 | 18.6 | 6.9 | 6.7 | 8.9 | 9.1 | 7.4 | 7.7 |
| Nd | 21.6 | 26.9 | 26.6 | 29.1 | 29.4 | 21.8 | 27.7 | 27.9 | 13.5 | 13.3 | 13.6 | 13.9 |
| Ni | 25 | 24 | 25 | 47 | 45 | 27 | 37 | 36 | 35 | 33 | 53 | 55 |
| Pb | 21.4 | 15.3 | 15.7 | 30.9 | 31.1 | 21.7 | 5.7 | 5.9 | 42.1 | 42.9 | 4.3 | 4.7 |
| Pr | 6.01 | 9.51 | 9.57 | 8.05 | 8.01 | 6.07 | 7.88 | 7.91 | 3.46 | 3.49 | 3.66 | 3.69 |
| Rb | 104 | 122 | 121 | 87 | 88 | 107 | 122 | 124 | 105 | 107 | 43 | 45 |
| Sm | 3.05 | 2.94 | 2.97 | 4.27 | 4.29 | 3.03 | 3.67 | 3.65 | 2.27 | 2.21 | 1.88 | 1.91 |
| Sn | 1.9 | 4.7 | 4.8 | 1.4 | 1.3 | 1.7 | 3.2 | 3.3 | 3.7 | 3.9 | 4.1 | 4.6 |
| Sr | 929 | 308 | 310 | 768 | 762 | 931 | 156 | 159 | 248 | 251 | 88 | 89 |
| Ta | 2.24 | 1.15 | 1.17 | 1.87 | 1.89 | 2.27 | 0.76 | 0.77 | 1.18 | 1.16 | 1.27 | 1.28 |
| Tb | 0.33 | 0.27 | 0.29 | 0.44 | 0.42 | 0.35 | 0.34 | 0.36 | 0.25 | 0.27 | 0.21 | 0.22 |
| Th | 15.8 | 12.8 | 12.7 | 13.7 | 13.9 | 16.1 | 13.7 | 13.9 | 15.1 | 15.3 | 11.1 | 11.3 |
| U | 4.53 | 5.31 | 5.33 | 5.66 | 5.57 | 4.56 | 3.06 | 3.09 | 7.52 | 7.48 | 8.24 | 8.26 |
| V | 59 | 58 | 61 | 81 | 83 | 61 | 16 | 72 | 67 | 69 | 79 | 82 |
| W | 2.3 | 5.4 | 5.5 | 4.2 | 4.4 | 2.2 | 4.4 | 4.6 | 12.8 | 12.9 | 21.7 | 21.4 |
| Y | 11.4 | 5.27 | 5.31 | 11.3 | 11.5 | 11.6 | 6.61 | 6.63 | 7.94 | 7.98 | 4.04 | 4.1 |
| Yb | 0.85 | 0.42 | 0.44 | 0.86 | 0.88 | 0.87 | 0.51 | 0.53 | 0.64 | 0.66 | 0.41 | 0.44 |
| Zn | 21.8 | 22.6 | 23.1 | 44.8 | 44.3 | 22.2 | 11.9 | 11.7 | 72.7 | 72.9 | 7.8 | 7.9 |
| Zr | 18 | 23 | 25 | 98 | 99 | 21 | 17 | 18 | 32 | 33 | 41 | 43 |
| Ge | | | | | | | | | | | | |
| In | | | | | | | | | | | | |
| Li | | | | | | | | | | | | |
| S | | | | | | | | | | | | |
| Sb | | | | | | | | | | | | |
| Se | | | | | | | | | | | | |
| Te | | | | | | | | | | | | |
| Tm | | | | | | | | | | | | |

**Table 6.** *Cont.*

| Sample | LAM1 | LAM2 | LAM3 | LAM4 | LAM5 | LAM6 | LAM7 | LAM8 |
|---|---|---|---|---|---|---|---|---|
| $SiO_2$ | 48.18 | 49.08 | 48.42 | 50.12 | 50.62 | 48.69 | 51.54 | 51.47 |
| $Al_2O_3$ | 13.04 | 13.82 | 13.6 | 13.62 | 13.96 | 13.48 | 13.77 | 13.74 |
| CaO | 1.37 | 3.31 | 5.23 | 3.41 | 3.42 | 4.96 | 3.62 | 3.74 |
| $Fe_2O_3$ | 4.39 | 3.82 | 3.88 | 3.87 | 5.3 | 5.61 | 5.65 | 5.32 |
| FeO | 5.91 | 5.32 | 4.7 | 5.02 | 5.3 | 4.59 | 5.22 | 5.32 |
| $K_2O$ | 6.69 | 4.67 | 6.6 | 4.61 | 4.72 | 6.42 | 5.17 | 4.92 |
| MgO | 8.27 | 7.26 | 7.58 | 7.44 | 8.34 | 8.54 | 7.38 | 7.57 |
| MnO | 0.01 | 0.02 | 0.04 | 0.03 | 0.03 | 0.04 | 0.03 | 0.04 |
| $Na_2O$ | 0.61 | 2.29 | 1.86 | 2.84 | 3.18 | 2.82 | 2.88 | 2.96 |
| $P_2O_5$ | 0.8 | 0.66 | 0.88 | 0.78 | 0.86 | 0.79 | 0.81 | 0.75 |
| $TiO_2$ | 0.71 | 0.65 | 0.86 | 0.78 | 0.67 | 0.89 | 0.76 | 0.84 |
| LOI | 3.61 | 4.02 | 3.82 | 3.67 | 3.71 | 3.82 | 3.98 | 3.66 |
| Total | 93.59 | 94.92 | 97.47 | 96.19 | 100.11 | 100.65 | 100.81 | 100.33 |
| Ag | 0.4 | 1.7 | 1.5 | 1.1 | 1.6 | 1.7 | 1.4 | 1.3 |
| As | 2.8 | 4.5 | 6.3 | 6.9 | 4.4 | 5.8 | 7.1 | 6.7 |
| Au | 0.08 | 0.09 | 0.07 | 0.08 | | | | |
| Ba | 870 | 673 | 814 | 981 | 282 | 396 | 562 | 524 |
| Be | 2.21 | 2.12 | 2.1 | 2.27 | 2.3 | 2.4 | 2.2 | 2.7 |
| Bi | 1.78 | 1.88 | 4.81 | 6.13 | 2.9 | 4.7 | 6.4 | 6.6 |
| Cd | 0.02 | 0.02 | 0.03 | 0.08 | 0.52 | 0.37 | 0.39 | 0.46 |
| Ce | 173 | 154 | 169 | 167 | 139 | 129 | 147 | 132 |
| Co | 15.6 | 15.9 | 16.1 | 21.2 | 15.7 | 16.8 | 20.7 | 19.5 |
| Cr | 322 | 273 | 280 | 288 | 178 | 185 | 162 | 182 |
| Cs | 5.54 | 3.12 | 4.61 | 5.12 | 1.7 | 1.4 | 2.3 | 1.9 |
| Cu | 3080 | 2245 | 2081 | 3121 | 2275 | 1988 | 1014 | 926 |
| Dy | 2.67 | 4.41 | 5.46 | 4.71 | 4.57 | 5.26 | 4.81 | 5.24 |
| Er | 1.1 | 1.82 | 2.32 | 1.78 | 1.92 | 2.13 | 1.98 | 2.16 |
| Eu | 2.11 | 1.87 | 2.43 | 2.53 | 1.97 | 2.23 | 2.83 | 2.37 |
| Ga | 25.7 | 26.4 | 24.9 | 29.1 | | | | |
| Gd | 5.13 | 7.75 | 9.79 | 9.03 | 7.85 | 9.46 | 9.24 | 9.16 |
| Hf | 2.1 | 1.9 | 2.29 | 1.8 | 0.82 | 1.19 | 0.86 | 0.93 |
| Ho | 0.46 | 0.51 | 0.47 | 0.49 | | | | |

**Table 6.** *Cont.*

| Sample | LAM1 | LAM2 | LAM3 | LAM4 | LAM5 | LAM6 | LAM7 | LAM8 |
|---|---|---|---|---|---|---|---|---|
| La | 86.4 | 78.6 | 80.9 | 79.6 | 74 | 89 | 76 | 82 |
| Lu | 0.12 | 0.13 | 0.15 | 0.11 | 0.15 | 0.13 | 0.12 | 0.16 |
| Mo | 2.35 | 3.88 | 2.95 | 2.91 | 3.78 | 2.99 | 2.86 | 2.75 |
| Nb | 18 | 30 | 38.2 | 38 | 35.6 | 38.9 | 37.4 | 36.7 |
| Nd | 66.9 | 60.7 | 67.3 | 65.8 | 61.9 | 67.6 | 66.8 | 65.7 |
| Ni | 138 | 85 | 113 | 121 | 89 | 93 | 129 | 124 |
| Pb | 6.9 | 11.9 | 8.6 | 6.2 | 35 | 34 | 28 | 31 |
| Pr | 19.1 | 17.3 | 18.1 | 17.9 | 17.29 | 18.42 | 17.93 | 17.68 |
| Rb | 210 | 182 | 202 | 195 | 216 | 192 | 207 | 189 |
| Sm | 8.91 | 8.69 | 9.01 | 8.41 | 7.45 | 8.96 | 8.54 | 8.21 |
| Sn | 4.8 | 5.9 | 6.2 | 4.9 | 5.7 | 6.4 | 4.8 | 5.2 |
| Sr | 198 | 468 | 494 | 435 | 465.8 | 496.4 | 437.3 | 442.6 |
| Ta | 0.84 | 1.02 | 0.98 | 1.16 | 3.29 | 3.68 | 3.74 | 2.56 |
| Tb | 0.54 | 0.76 | 0.95 | 0.84 | 0.79 | 0.95 | 0.87 | 0.83 |
| Th | 25.8 | 30.8 | 23.7 | 24.4 | 30.72 | 23.77 | 23.24 | 23.87 |
| U | 8 | 7.7 | 6.9 | 8.7 | 7.64 | 5.63 | 7.14 | 7.56 |
| V | 146 | 97 | 129 | 141 | 94 | 125 | 124 | 132 |
| W | 19.9 | 27.4 | 17.1 | 16.7 | 17.6 | 9.3 | 7.2 | 12.3 |
| Y | 11.4 | 11.6 | 14.3 | 11.8 | 11.6 | 13.5 | 12.4 | 12.7 |
| Yb | 0.8 | 0.9 | 1.1 | 0.8 | 0.8 | 1.2 | 0.9 | 1.3 |
| Zn | 7 | 17 | 19 | 15 | 26 | 37 | 45 | 36 |
| Zr | 72.4 | 81.6 | 77.4 | 92.3 | 88.6 | 102.7 | 71.2 | 79.4 |
| Ge | 0.31 | 0.28 | 0.36 | 0.32 | | | | |
| In | 0.07 | 0.14 | 0.35 | 0.24 | 0.17 | 0.26 | 0.31 | 0.29 |
| Li | 18.3 | 17.2 | 16.8 | 19.2 | 7 | 8 | 8 | 9 |
| S | 66,300 | 44,185 | 29,661 | 38,529 | 33,169 | 29,674 | 38,824 | 32,742 |
| Sb | 0.32 | 2.31 | 0.98 | 2.26 | 2.6 | 2.4 | 2.1 | 2.3 |
| Se | 17.1 | 12 | 13.7 | 15.6 | 2.24 | 1.27 | 1.66 | 1.72 |
| Te | 1.51 | 1.16 | 1.92 | 1.34 | 0.76 | 0.96 | 1.37 | 1.12 |
| Tm | 0.15 | 0.21 | 0.28 | 0.17 | 0.22 | 0.31 | 0.27 | 0.19 |

### 5.2.1. Trace Element Geochemistry

The chondrite-normalized rare earth element [39] patterns of the Sungun stock and post-mineralization dykes show a steep slope from light rare earth elements (LREE) (LaN/SmN = 6.80) to the heavy rare earth elements (HREE) ($Gd_N/Yb_N$ = 2.49) (Figure 13a), but do not have conspicuous Eu anomalies. Their primitive-mantle normalized trace element diagrams display enrichment in large ion lithophile elements (LILE) and depletion of high-field-strength elements (HFSE), with positive K, U, Pb, Nd, and Cs and negative Nb, P, Zr, Pr, and Ti anomalies, consistent with a subduction-related setting (Figure 13b). Their Nb, Ta, and Ti depletions are thought to be due to the absence of plagioclase and presence of Fe–Ti oxides (e.g., rutile) as residue in the source area of the parental magmas [40]; Nb and Ta depletion may also result from previous depletion events in the mantle source rocks [41,42]. Phosphorous also shows negative anomalies in the studied samples, which may be related to apatite fractionation. These chemical properties are analogous to those of the Sungun Porphyry.

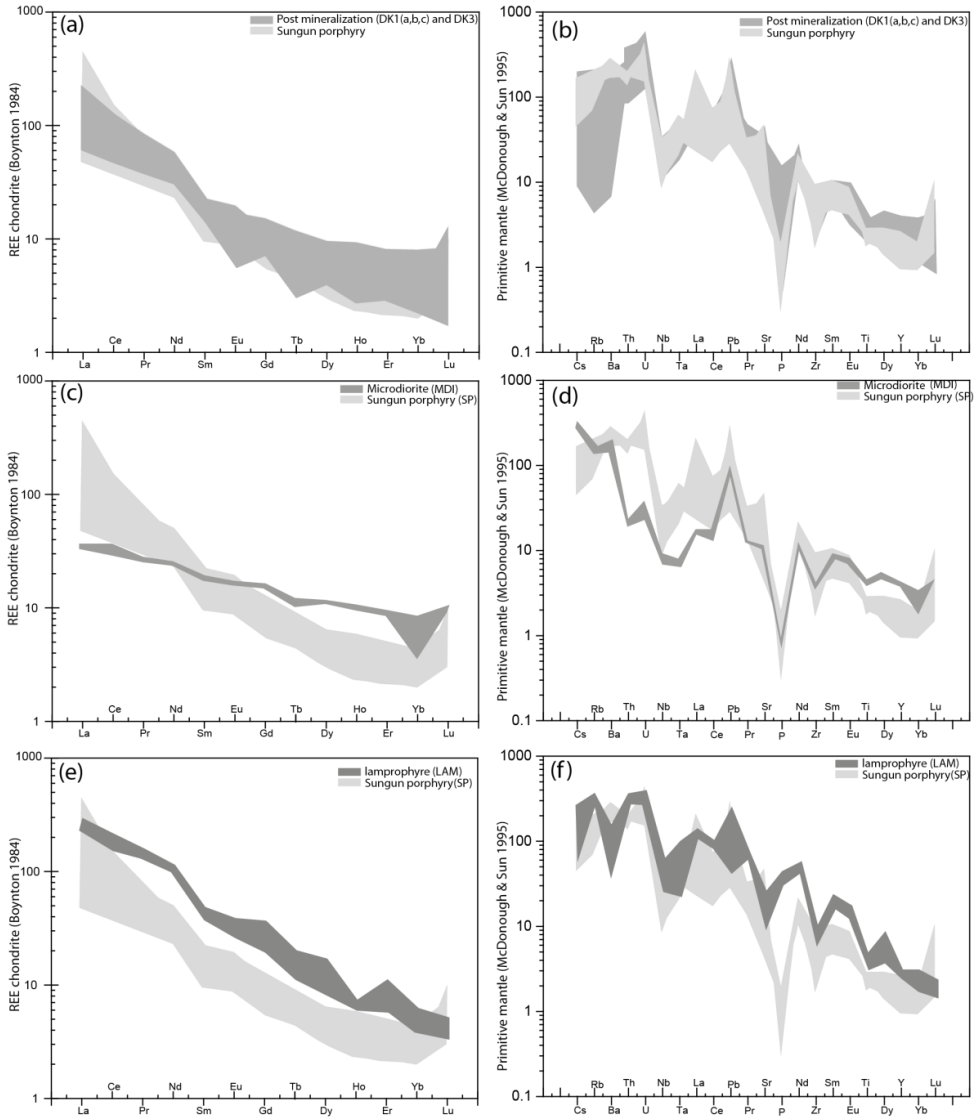


**Figure 13.** (**a**) Chondrite-normalized REE patterns for the quartz-monzonite stock, diorite and quartz diorite dykes [39]; (**b**) primitive mantle-normalized rare earth elements patterns for the quartz-monzonite stock, diorite and quartz diorite dykes [43]; (**c**) chondrite-normalized diagram [39] for the micro diorite dykes; (**d**) primitive mantle-normalized trace element diagram [43] for micro diorite dykes; (**e**) chondrite-normalised REE diagram for the lamprophyre dykes [39]; (**f**) primitive mantle-normalised multi element diagrams for the lamprophyre dykes [43].

Rare earth element (REE) chondrite-normalized patterns for microdiorite dykes are displayed in Figure 13c. Microdiorite dykes have LREE enrichment with weak negative Eu anomalies (Eu/Eu* = 0.93–0.97) and shallow HREE slope (Figure 13d). The minor negative Eu anomaly is likely related to the abundance and fractionation of plagioclase in the rocks. On a multi-element primitive mantle normalized diagram [43], microdiorite dykes show enrichments in most large ion lithophile elements (LILE), and a fairly regular depletion of high field strength elements (HFSE).

The chondrite-normalized REE patterns [43] of lamprophyres dykes are shown in Figure 13e. These show high REE abundances (ΣREE mostly within 317–367 ppm) and negative Eu anomalies (Eu/Eu* in the range 0.69–0.97) (Figure 13f).

### 5.2.2. Nd-Sr Isotopes

Sm–Nd and Rb–Sr isotopic data for six whole-rock samples of the mafic-intermediate dykes are provided in Table 7 and the initial epsilon values (20 Ma); calculations made with the $^{87}$Rb decay constant recommended by Reference [44] are illustrated in Figure 14. The $^{87}Sr/^{86}Sr$ ratios range from 0.704617 to 0.706464 and $^{143}Nd/^{144}Nd$ ratios range from 0.512648 to 0.512773.

**Table 7.** Results for Rb-Sr and Sm-Nd isotopic systems in samples of post-mineralization dykes from Sungun. Initial values were calculated for an age of 20 Ma, using the $^{147}$Sm decay constant of and the $^{87}$Rb decay constant of [45]. (* [25]).

| Sample | DK1a | DK1b | DK1c | DK3 | LAM | MDI | SP * 1 |
|---|---|---|---|---|---|---|---|
| Sr ppm | 608 | 725 | 662 | 298 | 198 | 234 | 681 |
| Rb ppm | 81.2 | 57.9 | 48.6 | 4.2 | 210 | 97.6 | |
| $^{87}Rb/^{86}Sr$ | 0.386 | 0.231 | 0.212 | 0.041 | 3.068 | 1.207 | 0.67497 |
| Error (2σ) | 0.011 | 0.007 | 0.006 | 0.001 | 0.087 | 0.034 | |
| $^{87}Sr/^{86}Sr$ | 0.704874 | 0.704619 | 0.704617 | 0.705151 | 0.705722 | 0.706801 | 0.704467 |
| Error (2σ) | $3.00 \times 10^{-5}$ | $2.70 \times 10^{-5}$ | $2.40 \times 10^{-5}$ | $2.10 \times 10^{-5}$ | $2.30 \times 10^{-5}$ | $3.40 \times 10^{-5}$ | |
| $(^{87}Sr/^{86}Sr)_i$ | 0.704766 | 0.704554 | 0.704558 | 0.705139 | 0.704864 | 0.706464 | |
| Nd ppm | 20.7 | 19.7 | 20.6 | 23.1 | 66.9 | 15 | |
| Sm ppm | 3.29 | 3.17 | 3.71 | 3.08 | 8.91 | 3.67 | |
| $^{147}Sm/^{144}Nd$ | 0.096 | 0.097 | 0.109 | 0.081 | 0.081 | 0.148 | 0.29235 |
| Error (2σ) | 0.005 | 0.005 | 0.006 | 0.004 | 0.004 | 0.008 | |
| $^{143}Nd/^{144}Nd$ | 0.512733 | 0.512767 | 0.512787 | 0.512659 | 0.512666 | 0.512767 | 0.51275 |
| Error (2σ) | $1.70 \times 10^{-5}$ | $1.70 \times 10^{-5}$ | $2.20 \times 10^{-5}$ | $1.70 \times 10^{-5}$ | $1.70 \times 10^{-5}$ | $1.70 \times 10^{-5}$ | |
| $(^{143}Nd/^{144}Nd)_i$ | 0.512721 | 0.512754 | 0.512773 | 0.512648 | 0.512655 | 0.512748 | |
| εNdi | 2.12 | 2.76 | 3.13 | 0.7 | 0.83 | 2.64 | |

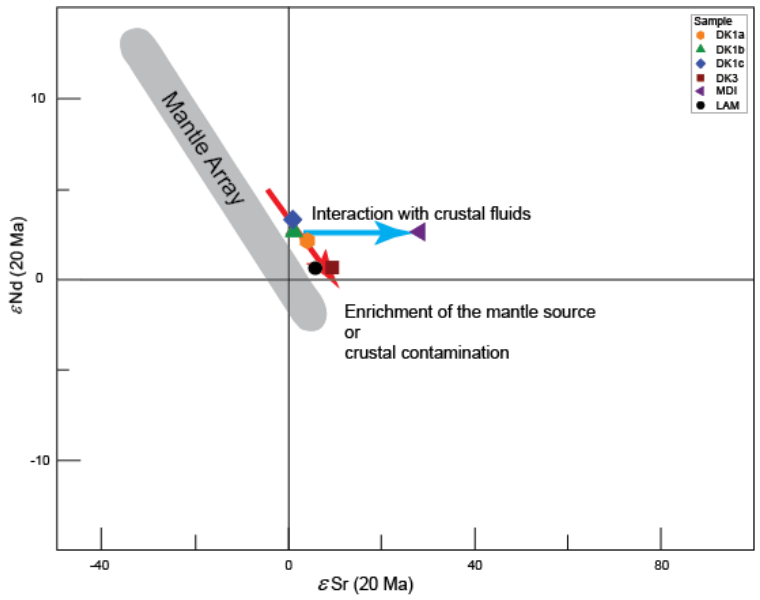


**Figure 14.** Plots of Sr–Nd isotopic compositions for the Sungun post-mineralization dykes. Initial values of εNdi vs. $^{87}Sr/^{86}Sri$ calculated for 20 Ma for the Oligo-miocene dykes [45].

The variations in the $^{87}Sr/^{86}Sr$ and $^{143}Nd/^{144}Nd$ ratios of the Sungun dykes DK1, DK3, MDI, and LAM is shown and compared with bulk Earth and the mantle array (Figure 14). Five samples from the quartz diorite, dacite, and lamprophyre dykes plot just to the right of the mantle array with a potential minor contribution from subduction derived fluid. The three DK1 samples plot very close to each other and are therefore likely to have a common origin. These three samples together with LAM and DK3 define a trend (red arrow on Figure 14).

The microdiorite dyke (MDI) has $^{87}Sr/^{86}Sr$ initial ratio of 0.706464, which is higher compared to the other samples (0.704554 to 0.705139) although its epsilon Nd value overlaps with those of the quartz-diorite (DK1) samples.

According to the study by reference [27], the Sungun porphyry stock and the post-mineralization dykes have unrelated origins. We show here, however, that based on trace elements and Sm-Nd isotopic results [27], the dykes intruding the Sungun stock are genetically related to the porphyry.

The similarity in trace element characteristics between the Sungun porphyry and diorite and quartz-diorite dykes within the area of the mine suggests that the dykes are comagmatic with the quartz-monzonite. The quartz diorite dykes are also isotopically associated to the Sungun Porphyry. Within the dyke suite a trend is seen from lower to higher $^{87}Sr/^{86}Sr$. This could have two most plausible explanations: (1) The samples would represent rocks whose parental magmas came from a progressively more enriched mantle compared to DK1c to DK3; or (2) assuming a single parental melt (in which case, DK1c is the sample that more closely represents its isotopic signature) the isotopic variation represent minor degrees of contamination, assimilation or mixing with crustal materials.

#### 5.2.3. Interpretations and Discussion

##### Tectonic Setting of the Sungun Stock and Post-Mineralization Dykes

Potassic rocks are found in several tectonic environments, such as cratons, post-collisional setting, and active orogenic belts and, to a lesser extent, oceanic intraplate settings [46] and have moderate abundances of LREE, LILE, and HFSE [47]. Shoshonitic rocks in particular are associated with many continental and oceanic arcs [48]. The tectonic affinities of ancient and altered/mineralized rocks can be investigated with the use of immobile trace elements. A significant feature of volcanic arc magmatism is the depletion in HFSE relative to other incompatible elements as well as their LILE enrichment (e.g., [49,50]). At Sungun the average Ba/Nb and Rb/Nb ratios are 37.5 and 10.5 in felsic dykes and 62.5 and 7.6 in the intermediate-mafic dykes, respectively, which is a feature of arc environments [51]. The Th/Yb versus Ta/Yb diagram [52] highlights the Shoshonitic character of the Sungun rocks with the Th enrichment indicative of subduction fluids input (Figure 15a). Based on the diagram of [53], high Th/Yb ratios correlated with high values for La/Yb are consistent with continental arc magmas (Figure 15b), in agreement with the Y vs. Zr plot (Figure 15c). Based on the $Ce/P_2O_5$ vs. $Zr/TiO_2$ diagrams of [47] the studied samples plot in the post-collisional arc related fields (Figure 15d).

In summary, the combination of field, petrographic and geochemical data of the Sungun stock and post-mineralization dykes shows that they formed during a post-collisional stage. This is in agreement with previous reports on the petrogenesis of igneous rocks in the Urumieh-Dokhtar magmatic belt [54–56]. Indeed, recent tectono-magmatic reviews have suggested that the Eocene magmatic event may have been a consequence of the geometrically complex subduction of the Neotethys oceanic crust underneath Central Iran, with the Sungun post-mineralization dykes intruding in the late stages of continental collision. The negative Eu anomalies can be generated by melting of a source rich in residual feldspar and/or plagioclase fractionation during ascent and emplacement of these intrusions [57]. The steep REE slope on the other hand is indicative of residual garnet in in the mantle source [58,59], hence precluding the presence of plagioclase as the aluminous phase in the mantle. The generally steep REE slope of the multi-element patterns is also typical of lamprophyres generated by small degrees of partial melting. The primitive mantle-normalized patterns of lamprophyre dykes (Figure 13f) show the characteristic enrichments in Th, Rb, K, Pb, Nd, Sm, and Dy, and depletion in Ba,

Ce, Nb, Ta, Sr, Zr, and Ti, which are compatible with a geodynamic environment involving subduction zone magmatism [60]. This enrichment in incompatible elements implies that the melt source from which the magmas were derived was likely to be metasomatized lithospheric mantle enriched in K and incompatible elements [61].

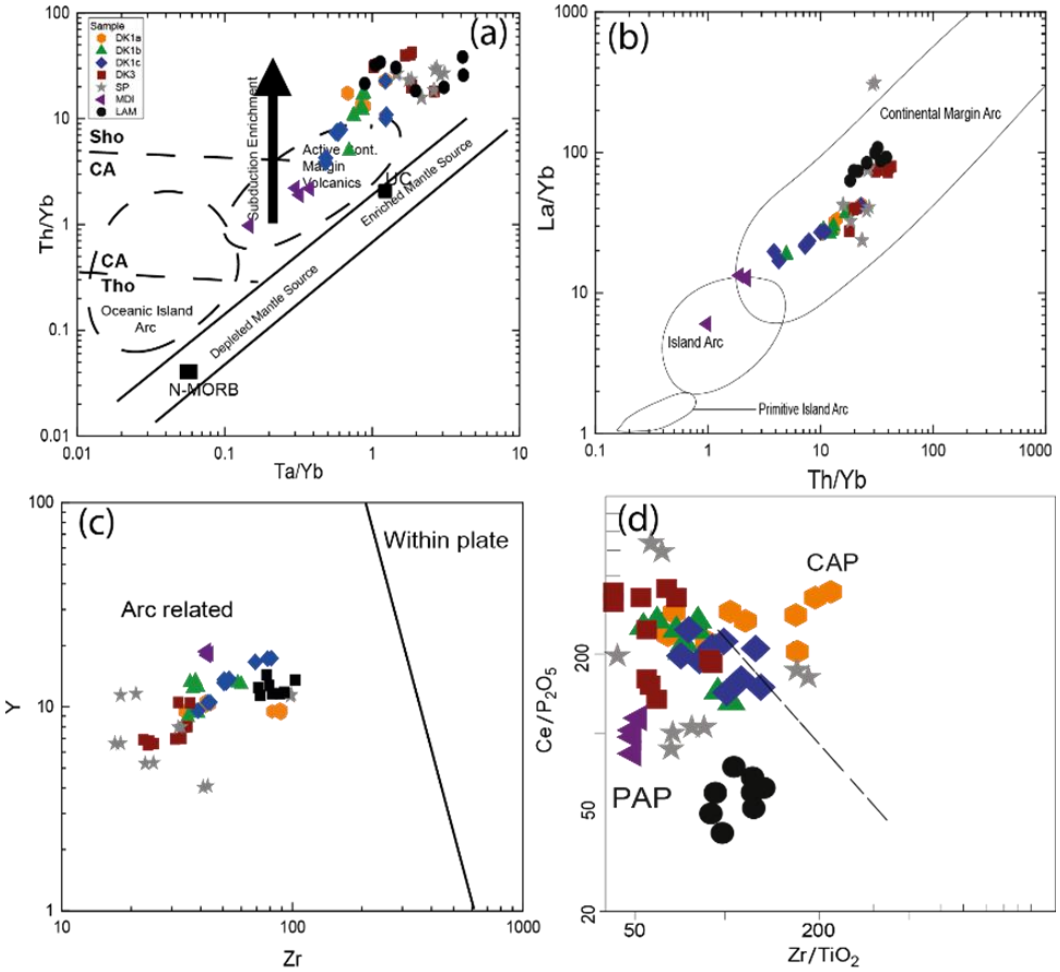


**Figure 15.** (**a**) Th/Yb vs. Ta/Yb diagram [52] for the Sungun post mineralization dykes. Tho is tholeiitic, CA is calc-alkaline, Sho is shoshonitic; (**b**) La/Yb vs. Th/Yb geotectonic discrimination diagram after [53]. The sungun stock and late dykes plot in the Continental Margin Arc fields; (**c**) Y vs. Zr geotectonic discrimination diagrams of [47], for within-plate and from arc related and (**d**) $Ce/P_2O_5$ vs. $Zr/TiO_2$ geotectonic discrimination diagrams of Reference [47], samples plot mostly in the PAP field. PAP is post collision arc and CAP is active continental margin.

Petrogenesis of Quartz Monzonite Stock, Quartz Diorite and Diorite Dykes

The $^{87}Sr/^{86}Sr$ and $^{143}Nd/^{144}Nd$ vs. $SiO_2$ diagrams of the Sungun dykes are used to examine any roles of crustal contamination superposed to the principal fractional crystallization control of magmatic evolution. The isotope ratios do not show any obvious correlation with $SiO_2$ contents (Figure 16a,b) and incompatible elements abundance, such as Th (Figure 16c). Hence, we suggest that crustal assimilation did not play an important role during the magmatic evolution of the quartz diorite and diorite magmas, whereas the high $^{87}Sr/^{86}Sr$ of the microdiorite dykes suggests that it may have been affected by such processes.

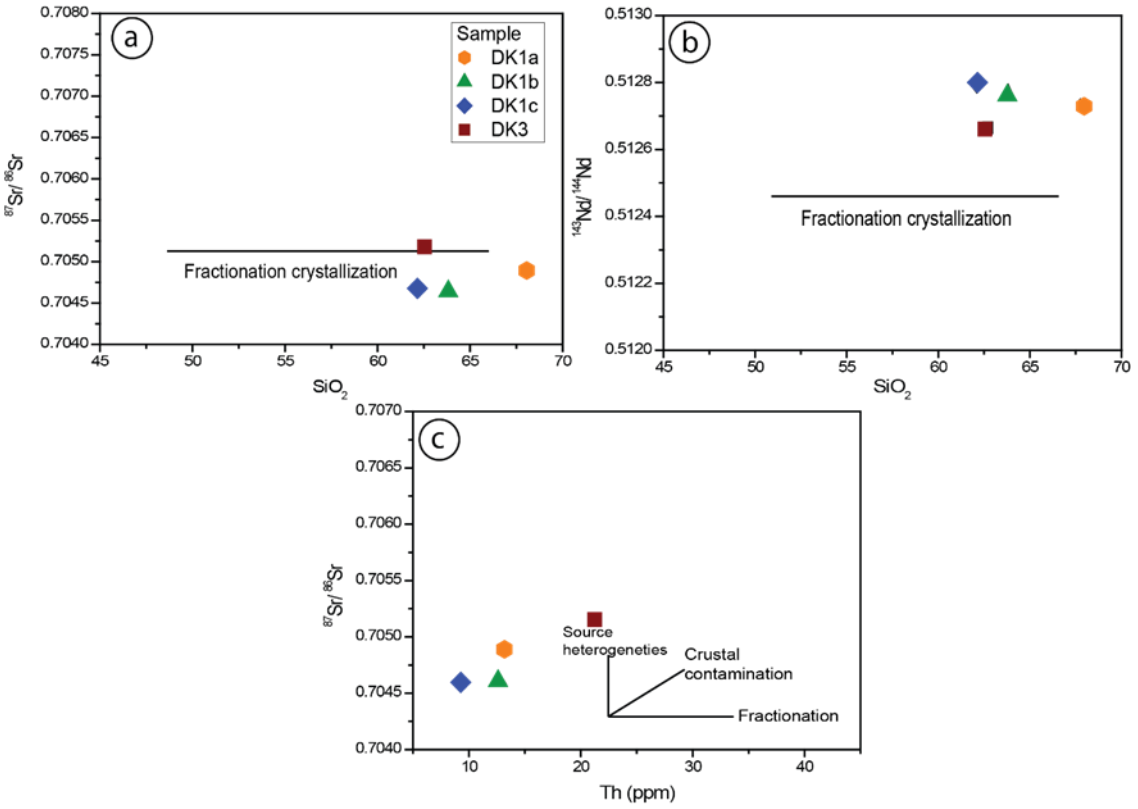


**Figure 16.** Variation diagrams. (**a**) $^{87}Sr/^{86}Sr$ versus $SiO_2$; (**b**) $^{143}Nd/^{144}Nd$ vs. $SiO_2$; and (**c**) $^{87}Sr/^{86}Sr$ versus Th [62].

To determining the degree of enrichment or depletion in the samples from the study area we used the ratios of incompatible elements Y vs. Zr [63] (e.g., Figure 15c). These elements are useful to interpret the petrogenesis of igneous rocks, even in highly altered rocks, due to their very low mobility [64]. Based on their incompatible element characteristics (Figure 15) the magma of Sungun porphyry and post-mineralization dykes originated from mantle enriched by subduction processes.

Previous studies on the genesis and evolution of Neotethys show the different opening ages. Different ages are due to uncertainty in the transition from extensional tectonics to the onset of contraction. Moreover, different researchers considered the time for oceanic closing and collision events to range from upper Cretaceous-Paleocene (Laramie phase) [55,65,66], Oligocene [67], and late Miocene-Pliocene [68–71]. Due to these complexities in Neotethys evolution more data are needed to clarify its tectonic history and particularly its closing stages.

It can be said, in summary, that some researchers have related the Neotethys closing to the upper Cretaceous, emphasizing the oceanic extension from the Kermanshah to the Esphandeqeh and Neyriz [65]. They relate the Eocene and Oligocene magmatic activities of Central Iran and the Alborz-Azerbaijan crust to the tectonic and petrogenetic evolution after the collision [65].

On the other hand, other researchers do not consider the origin of the Upper Cretaceous Ophiolite mélanges as resulting from collision of the Arabia plate with Iran. They argue this because Ophiolite mélanges are also present in Makran, where there is continent collision and the subduction is still ongoing. S-type granites, such as the Alvand Granite, adjacent to the ophiolites strongly support collision occurrence and end of subduction in this area, whereas no S-type granites occur in the Makran area. Considering these evidences it can be argued that this extended basin with NW-SE trend, closed during the Upper Cretaceous and Laramie phase of the Arabia Plate and Iran block collision. After that, during the Pyrenean phase, various fractures have been created in Central Iran, Alborz, and Azerbaijan while subduction fluids influenced the mantle wedge [6] imparting a clear subduction geochemical signature on it. In the last stages of Arabian Plate and Iran block convergence, the

Pyrenean phase induced a strong compressive regime, which caused early formed mafic melts to pond in the crust, providing favourable conditions for melting the thick continental crust and generating hybrid magmas [65].

The sialic back arc basins contracted after the closing of the main oceanic basin, causing the generation of thrusts and inverse faults [65]. Subsequently these basement fractures were reactivated in Central Iran during tensional events. This caused localized upwelling in the metasomatized mantle wedge, leading to partial melting that formed the Tertiary magmatism of the Urmia-Dokhtar and Alborz-Azerbaijan zones. Due to the subduction, Neotethys Ocean closing and the post collision processes, several porphyry copper deposits were formed [65]. The important Iran copper belt (Urmia-Dokhtar), contains volcanic and plutonic rocks and extends in a NW-SE direction. Its SE and NW extensions are known as the Kerman copper belt and Arasbaran copper belt, respectively.

The Sungun porphyry stock and associated dykes were derived from partial melting in the lithospheric mantle metasomatised and enriched by the release of fluids from the Neothetys oceanic crust and subducted pelagic sediments, causing enrichment of LILE and LREE and depletion of HFSE. Sr and Nd isotopic data, as well as trace elements, indicated magmas feeding the post-mineralization dykes were generated in the LILE and LREEe enriched lithospheric mantle. Magma generation and ascent was therefore likely promoted by tectonic tensions after continental collision.

Based on the overall trace element and isotopic similarities, we consider that the Sungun Porphyry and dioritic dykes (DK1 and DK3) all evolved from a common parent melt. Thermo-barometric models [28] of the dioritic parent suggest the presence of a magma chamber at a maximum of 19 kbar (approximately from 57 to 60 km). Secondary magma chambers existed up to depth of 12–14 km (6 kbar), where magma underwent gravity settling and differentiation [28].

The chemical composition of younger dykes is more mafic than older ones. The more felsic member of the magmatic system is represented by the Sungun quartz-monzonite (SP) porphyry, and was likely the more evolved and higher portion of a layered magma chamber (Figure 17). The more mafic member, DK3, was being stored at the base of the chamber. The DK1 magma represent intermediate levels within the layered magma chamber (Figures 18 and 19), which were extracted after the emplacement of the Sungun porphyry, and prior to the emplacement of the lower mafic portion as DK3 dykes.

### Petrogenesis of Lamprophyre Dykes

Lamprophyre dykes cross cut the Sungun copper deposit and various other rock units. According to the results of borehole logging in this mine and geothermometry results [29], these dykes were intruded at least after the Oligo-Miocene. In order to evaluate the source of magma, and the degree of partial melting of the mantle, we can use a diagram of La/Sm vs. La [72] (Figure 18). All the samples have a high La/Sm ratio, which is consistent with an enriched mantle source, and less than 5% partial melting of garnet-lherzolite (Figure 18a). Trace elements can also give us information on the influence of hydrous mineral phases on the melting process, as elements such as Ba and Rb are compatible in phlogopite, whereas Ba, Sr, Rb, are only moderately compatible in amphibole [59]. As a consequence, melts in equilibrium with phlogopite will have high values of the Rb/Sr and lower values of Ba/Rb compared to melts in equilibrium with amphibole (Figure 18b). The data illustrate how the lamprophyre magma was likely formed from mantle with residual phlogopite.

The lamprophyre dykes are homogeneously characterized by high abundances of incompatible trace elements (LILE and LREE) and they are distinguished by significant negative Ti, Zr, Sr, Ta, Nb, and Ba anomalies (Figure 13e,f), indicating that they were not derived from normal MORB or OIB source mantle (e.g., [73,74]). Moreover, the average Ce/Pb ratios (~11) of the most primitive samples are considerably different from those of oceanic basalts (~25; [75]), suggesting that these rocks are not derived from normal asthenospheric mantle.

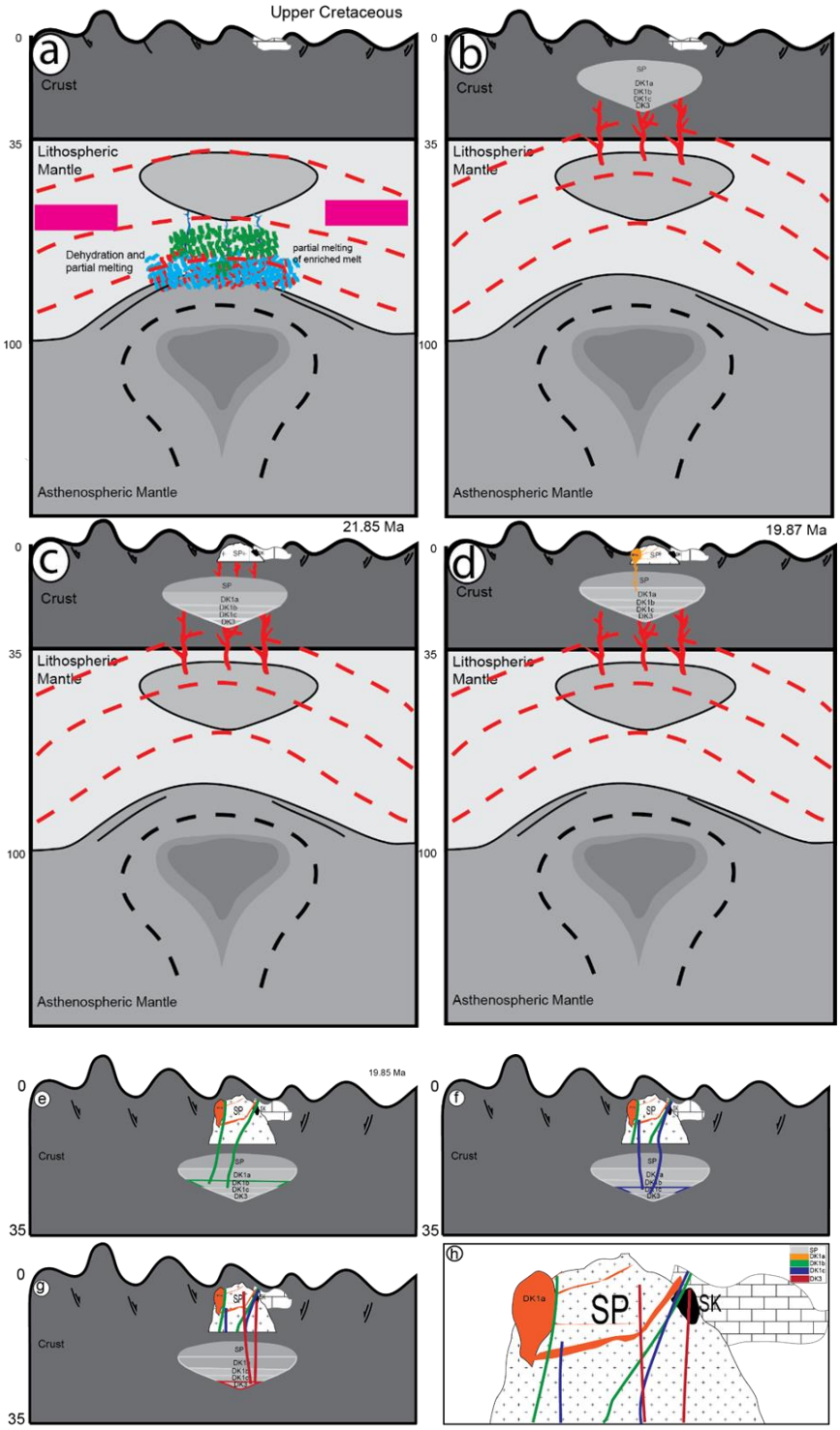


**Figure 17.** Model showing the Three-stage emplacement of the post-mineralization dykes. (**a**,**b**) Neotethys closure in the upper Cretaceous and the onset of metasomatism in the asthenosphere and the lithosphere; (**c**) enplacement of the Sungun Porphyry 21 million years ago; (**d**) injection of the first (DK1a) and oldest post-mineralization dykes; (**e**–**h**)Simplified cartoons showing the geodynamic and petrogenetic evolution of the post-mineralization dykes within the Sungun porphyry deposit. (**e**) quartz diorite dykes injection in the Sungun porphyry; (**f**) further injection of quartz diorite dykes; (**g**) the emplacement of the inclusion-rich quartz diorite; and (**h**) schematic diagram shows the post-emplacement geometry (cross-section) of the Sungun porphyry and post mineralization dyke in Varzaghan, NW Iran.

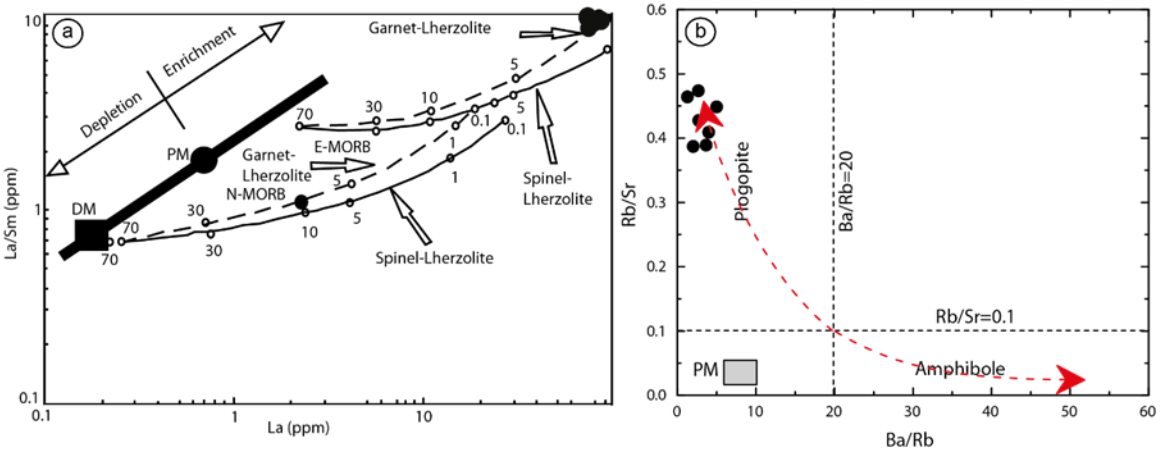


**Figure 18.** (**a**) Plots of La/Sm vs. La showing modeling of REE abundances and ratios to constrain the source characteristics of the alkaline magma in terms of REE concentrations, source mineralogy and degree of partial melting [72]. The continuous and dashed lines represent different values of partial melting of spinel- and garnet-lherzolite mantle respectively. The lines have numbers indicating the degree of partial melting. Models run for N-MORB and E-MORB; and (**b**) variations in Rb/Sr vs. Ba/Rb ratios that may constrain source mineralogy [59].

Furthermore, reference [76] as well as reference [77] showed that HFSEs such as Nb and Ta are depleted in the lithospheric mantle compared to LREEs. For instance, the ratio of Nb/La > 1, indicates an OIB-like asthenospheric mantle source for basaltic magmas, whereas a ratio lower than 0.5 indicate a lithospheric mantle source (Figure 19). In the Sungun calc-alkaline Lamprophyres Nb/La is between 0.49 and 0.20, confirming their origin from the lithospheric mantle. On the other hand, the low amount of Nb/La may be a consequence of mantle metasomatism by subduction fluids, introducing more La with respect to Nb due to its greater mobility in subduction fluids.

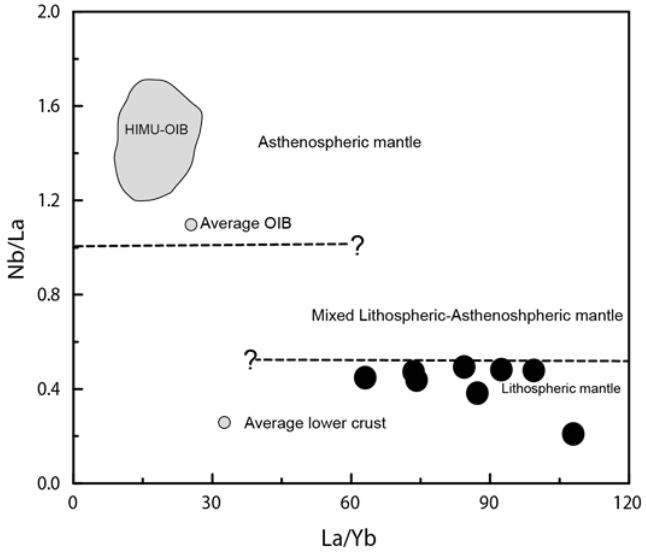


**Figure 19.** Nb/La versus La/Yb variation diagram. Average OIB is after [51] and average lower crust is after Reference [78]. Dashed lines separating fields of the asthenospheric, lithospheric and mixed mantle are plotted based on data given in Reference [77]. The HIMU-OIB area is reported in Reference [79].

Overall the major and trace elements and Sr–Nd isotopic characteristics of lamprophyre dykes are similar to previously intruded SP and post-mineralization dykes, suggesting they derived from a similar source. Our data suggests that the lamprophyres dyke originated from a low degree of partial

melting of an enriched lithospheric mantle source and were emplaced in a post collisional tectonic setting. The fluxing of the mantle wedge by the subduction fluids caused the formation of phlogopite, which was likely a residual phase during melting to form the lamprophyre.

Petrogenesis of Microdirite Dykes

Isotope data of the microdiorite (MDI) sample are typical of rocks that underwent hydrothermal alteration, which may affect the Sr isotopic signature without changing the Nd isotopic ratio. Therefore, the MDI parental melt could have derived from the same mantle source as the quartz diorite (DK1) samples, but the rock could have been subjected to hydrothermal alteration, causing an enrichment in crustal Sr (with higher $^{87}Sr/^{86}$ Sr) and the shift to the right on the Nd-Sr isotopic diagram (blue arrow in Figure 14).

The chemical composition of magma can be modified through assimilation of crustal materials during ascent and storage leading to the modification of selected trace element ratios diagnostic of arc and subduction environments. The microdiorite (MDI) dykes cross cutting the Sungun stock have high Ba/Nb (>28), which is a common feature of arc magmas (e.g., Reference [51]), and high La/Nb ratios (1.9–2.30) indicating crustal involvement [80]. Furthermore, prevalent low Ce/Pb (1.64–2.1), Rb/Ba, Nb/U, Nb/Y, and high La/Nb and La/Ta ratios also suggest lithospheric contributions. On primitive mantle-normalized multi-element diagrams, however, MDI dykes have similar signatures to those of the Sungun stock and other late dykes (Figure 13). Menzies et al. [81] have argued that Zr/Ba values can be used to distinguish lithospheric (0.3–0.5) from asthenospheric sources (Zr/Ba 0.5–0.7). The microdirite dykes have low Nb/La (0.43–0.51) and high Ba/Nb (172–269) values, but their Zr/Ba ratios (0.03–0.04) suggest generation from the lithospheric sources. Therefore, these observed differences may instead result from heterogeneous chemical composition in the source region, or changes in melting degree or post-crystallization alteration, rather than the direct crustal involvement.

Other chemical parameters can be used to assess the levels of crustal contamination. For example, basaltic rocks have been affected by crustal contamination have ratios La/Ta > 22 and La/Nb > 1.5 [82]. These ratios in the studied microdioritic dykes are 34–41 and 1.90–2.30, respectively, suggesting the influence of crustal contamination.

## 6. Conclusions

The mineralized porphyry and post-mineralization dykes at Sungun have a composition of quartz-monzonite, quartz diorite, gabbrodiorite, microdiorite, granodiorite, and lamprophyre. Generally, the post-mineralization dykes of the Sungun copper mine are subdivided into eight groups based on relative time of intrusion and into six groups according to their composition. The dykes trend sub-parallel to joints within the mine area, indicating intrusion and emplacement of dykes within previous fractures and crustal weaknesses.

Our data allowed us to relate all the igneous rocks occurring within the Sungun Cu-Mo mine area. The Sungun quartz-monzonite can be related through fractional crystallization processes to the quartz diorite and diorite dykes as they all have analogous chemical characteristics, such as light rare earth elements enrichment and HFSE depletion, and have similar Sr-Nd isotopic ratios. We propose a scenario where these intrusions belong to a single magmatic system that evolved in the middle crust. The mineralized Sungun porphyry was the first to be emplaced in the upper crust, with associated fluids forming Cu-Mo mineralization. Further portions of the evolving magmatic system were subsequently injected as dykes, becoming progressively more mafic with time due to the tapping of a zoned magma chamber.

Microdiorite and lamprophyric dykes are also related to the sample geodynamic environment as they share similar subduction signatures, such as depletion of Nb, Ta, and Ti. These dykes were intruded at a later stage. The microdiorite magma had a greater influence of crustal contamination compared to the other Sungun suite. The lamprophyre magma was likely derived from residual low-degree melts in equilibrium with mantle phlogopite, following the main subduction-related pulse.

**Author Contributions:** A.A.K. and M.M. performed fieldwork, analyses and drafted the paper, N.A. and M.R.H. contributed with analytical techniques; K.M. contributed to writing, reviewing and editing the paper; J.F.S. provided analytical data; M.B. provided comments and edited the paper.

**Funding:** Financial support was provided by University of Tabriz, Iran, National Iranian Copper Industries Company (NICICO) and by the Iranian Mineral Processing Research Center (IMPRC) Fund.

**Acknowledgments:** Jamshid Ahmadian is thanked for help with Electron Microprobe analyses. We thank the Sungun Copper Mine authorities and especially Golchin, competent geologist, for providing us with comprehensive data for this study, and Hamid Norouzi of Parsolang Engineering Consultant Company for supporting this project with the needed geological data. We would like to thank two anonymous reviewers for providing constructive reviews.

**Conflicts of Interest:** The authors declare no conflicts of interest.

## References

1. Haghipour, A.; Saidi, A.; Aganabati, A. *International Geological Map of the Middle East 1:5,000,000*, 2nd ed.; Geological Survey of Iran (GSI) and Commission of the Geological Map of the World (CGMW); UNESCO: Paris, France, 2009.
2. Berger, B.R.; Ayuso, R.A.; Wynn, J.C.; Seal, R.R. Preliminary model of porphyry copper deposits. *US Geol. Surv. Open File Rep.* **2008**, *1321*, 55.
3. Zürcher, L.; Bookstrom, A.A.; Hammarstrom, J.M.; Mars, J.C.; Ludington, S.; Zientek, M.L.; Dunlap, P.; Wallis, J.C.; Drew, L.J.; Sutphin, D.M.; et al. *Porphyry Copper Assessment of the Tethys Region of Western and Southern Asia: Chapter V in Global Mineral Resource Assessment*; US Geological Survey: Reston, VA, USA, 2015.
4. Leaman, P.; Staude, J.M. *Metallogenic evolution of the Western Tethys of Turkey and Iran*; Metal Mining Agency of Japan, Mineral Resources Information Center: Tokyo, Japan, 2002; pp. 15–16.
5. Calagari, A.A. Stable isotope (S, O, H and C) studies of the phyllic and potassic–phyllic alteration zones of the porphyry copper deposit at Sungun, East Azarbaidjan, Iran. *J. Asian Earth Sci.* **2003**, *21*, 767–780. [CrossRef]
6. Hezarkhani, A. Petrology of the intrusive rocks within the Sungun porphyry copper deposit, Azerbaijan, Iran. *J. Asian Earth Sci.* **2006**, *27*, 326–340. [CrossRef]
7. Richards, J.P.; Sholeh, A. The Tethyan tectonic history and Cu-Au metallogeny of Iran. *Econ. Geol. Spec. Publ.* **2016**, *19*, 193–212.
8. Moshefi, P.; Hosseinzadeh, M.R.; Moayyed, M.; Lentz, D.R. Comparative study of mineral chemistry of four biotite types as geochemical indicators of mineralized and barren intrusions in the Sungun Porphyry Cu-Mo deposit, northwestern Iran. *Ore Geol. Rev.* **2018**, *97*, 1–20. [CrossRef]
9. Sillitoe, R.H. Porphyry copper systems. *Econ. Geol.* **2010**, *105*, 3–41. [CrossRef]
10. Maanijou, M.; Mostaghimi, M.; Abdollahi Riseh, M.; Sepahi, A.A. Systematic sulfur stable isotope and fluid inclusion studies on veinlet groups in the Sarcheshmeh porphyry copper deposit: Based on new data. *J. Econ. Geol.* **2012**, *4*, 217–239.
11. Mohammadi Laghab, H.; Taghipour, N.; Iranmanesh, M.R. Distribution pattern of Cu, Mo, Pb, Zn and Fe elements in Sara (Parkam) porphyry copper deposit, Shahr–Babak, Kerman Province. *Iran J. Geol.* **2012**, *5*, 17–28.
12. Ravankhah, A.; Moayyed, M.; Amini, S.; Hosseinzadeh, G.H.; Hemmatjoo, A. Studies of geology, petrology, economic geology and alteration zones in porphyry copper deposit of Dareh-zar (southwest of Kerman). *Iran J. Geol.* **2010**, *3*, 63–75.
13. Moayyed, M. *Geological and Exploration Operations Report of Haftcheshme Copper Deposit*; National Copper Company of Iran and Pars Olang Engineering Consultant Company: Tehran, Iran, 2008.
14. Etminan, H. A porphyry copper-molybdenum deposit near the Sungun village. *Iran. Geol. Surv. Intern. Rep.* **1977**, *1*, 24.
15. Emami, M.; Babakhani, A. Studies of geology, petrology, and litho-geochemistry of Sungun Cu–Mo deposit. *Iran Minist. Mines Met.* **1991**, *61*, 50–63.
16. Gaderi, M. Economic Geology Study of Sungun Copper Copper Deposit. Master's Thesis, Shahid Beheshti University, Tehran, Iran, 1991.

17. Mehrpartou, M. Contributions to the Geology, Geochemistry, Ore Genesis and Fluid Inclusion Investigations on Sungun Cu-Mo Porphyry Deposit (North-West of Iran). Ph.D. Thesis, University Hamburg, Hamburg, Germany, 1993.
18. Izadyar, J. The Study of Petrography and Petrology of Igneous Rocks Sungun Deposit Area. Master's Thesis, Shahid Beheshti University, Tehran, Iran, 1995.
19. Calagari, A.A. Geochemical, Stable Isotope, Noble Gas and Fluid Inclusion Studies of Mineralization and Alteration at Sungun Porphyry Copper Deposit, East Azarbaidjan, Iran: Implications for Genesis. Ph.D. Thesis, University of Manchester, Manchester, UK, 1997.
20. Hezarkhani, A.; Williams-Jones, A.E. Controls of alteration and mineralization in the Sungun porphyry copper deposit, Iran; evidence from fluid inclusions and stable isotopes. *Econ. Geol.* **1998**, *93*, 651–670. [CrossRef]
21. Calagari, A. Concentration Variations of Major and Minor Elements across Various Alteration Zones in Porphyry Copper Deposit at Sungun, East Azarbaidjan, Iran. *J. Sci. Islam. Repub. Iran* **2003**, *14*, 27–36.
22. Calagari, A.A.; Hosseinzadeh, G. The mineralogy of copper-bearing skarn to the east of the Sungun-Chay river, East-Azarbaidjan, Iran. *J. Asian Earth Sci.* **2006**, *28*, 423–438. [CrossRef]
23. Moayyed, M. *Petrographic and Mineralographic Report of Sungun Copper Deposit*, 1st ed.; Pars Olang Engineering Company: Tehran, Iran, 2004.
24. Hamedi, A. *Study of Sungun Porphyry Copper Deposit Structures with a Particular Perspective on the Administration and Distribution Mechanisms of Dykes, in GEOLOGY*; University of Tabriz: Tabriz, Iran, 2007.
25. Hassanpour, S. Metallogeny and Mineralization of Copper and Gold in Arasbaran Zone (Eastern Azerbaijan) in Geology. Ph.D. Thesis, Shahid Beheshti University, Tehran, Iran, 2010.
26. Alavi, G. Study of the Skarn Deposits Around the Sheyvar-Dagh Batolith and Comparision with the Sungun Porphyry Skarn, in Geology. Ph.D. Thesis, University of Tabriz, Tabriz, Iran, 2014.
27. Aghazadeh, M.; Hou, Z.; Badrzadeh, Z.; Zhou, L. Temporal–spatial distribution and tectonic setting of porphyry copper deposits in Iran: Constraints from zircon U–Pb and molybdenite Re–Os geochronology. *Ore Geol. Rev.* **2015**, *70*, 385–406. [CrossRef]
28. Kamali, A. Petrology and Mineral Chemistry of Post Mineralization Dykes of SUNGUN Cu-Mo Porphyry Deposit, North of Varzegan, East Azerbaijan. Ph.D. Thesis, University of Tabriz, Tabriz, Iran, 2016.
29. Kamali, A.; Moayyed, M.; Amel, N.; Hosseinzadeh, M. Mineral chemistry and geochemistry of lamprophyric dykes in the Sungun Cu–Mo porphyry deposit (Varzaghan–Northwestern Iran). *Geosci. Sci. Q. J.* **2017**, *26*, 73–90.
30. Kamali, A.; Mohsen, M.; Amel, N.; Hosainzadeh, M. Mineralogy and mineral chemistry of quartz-dioritic dykes of Sungun Mo–Cu porphyry deposit (NW Iran). *Iran. J. Crystallogr. Miner.* **2017**, *25*, 123–138.
31. Deer, W.A.; Howie, R.A.; Zussman, J. *An Introduction to the Rock-Forming Minerals*; Longman Scientific & Technical: Hong Kong, 1992; Volume 2.
32. Leake, B.E. Nomenclature of amphiboles. *Miner. Mag.* **1978**, *49*, 533–563. [CrossRef]
33. Leake, B.E.; Woolley, A.R.; Arps, C.E.; Birch, W.D.; Gilbert, M.C.; Grice, J.D.; Hawthorne, F.C.; Kato, A.; Kisch, H.J.; Krivovichev, V.G.; Linthout, K. Nomenclature of amphiboles: Report of the subcommittee on amphiboles of the international mineralogical association commission on new minerals and mineral names. *Miner. Mag.* **1997**, *61*, 295–321. [CrossRef]
34. Rieder, M.; Cavazzini, G.; D'yakonov, Y.S.; Frank-Kamenetskii, V.A.; Gottardi, G.; Guggenheim, S.; Koval', P.V.; Mueller, G.; Neiva, A.M.; Radoslovich, E.W.; et al. Nomenclature of the micas. *Clays Clay Miner.* **1998**, *46*, 586–595. [CrossRef]
35. Winchester, J.; Floyd, P. Geochemical discrimination of different magma series and their differentiation products using immobile elements. *Chem. Geol.* **1977**, *20*, 325–343. [CrossRef]
36. Pearce, J.A. Trace element characteristics of lavas from destructive plate boundaries. *Andesites* **1982**, *8*, 525–548.
37. Rock, N.M.S. The nature and origin of lamprophyres: An overview. *Geol. Soc. Lond. Spec. Publ.* **1987**, *30*, 191–226. [CrossRef]
38. Bergman, S.C. Lamproites and other potassium-rich igneous rocks: A review of their occurrence, mineralogy and geochemistry. *Geol. Soc. Lond. Spec. Publ.* **1987**, *30*, 103–190. [CrossRef]
39. Boynton, W.V. Cosmochemistry of the rare earth elements: Meteorite studies. In *Developments in Geochemistry*; Henserson, P., Ed.; Elsevier: Amsterdam, The Netherlands, 1984; Volume 2, pp. 63–114. [CrossRef]

40. Martin, H. Adakitic magmas: Modern analogues of Archaean granitoids. *Lithos* **1999**, *46*, 411–429. [CrossRef]
41. Woodhead, J.; Eggins, S.; Gamble, J. High field strength and transition element systematics in island arc and back-arc basin basalts: Evidence for multi-phase melt extraction and a depleted mantle wedge. *Earth Planet. Sci. Lett.* **1993**, *114*, 491–504. [CrossRef]
42. Gust, D.A.; Arculus, R.J.; Kersting, A.B. Aspects of magma sources and processes in the Honshu arc. *Can. Miner.* **1997**, *35*, 347–365.
43. McDonough, W.F.; Sun, S.-S. The composition of the Earth. *Chem. Geol.* **1995**, *120*, 223–253. [CrossRef]
44. Villa, I.M.; De Bièvre, P.; Holden, N.E.; Renne, P.R. IUPAC-IUGS recommendation on the half-life of 87 Rb. *Geochim. ET Cosmochim. Acta* **2015**, *164*, 382–385. [CrossRef]
45. Zindler, A.; Hart, S. Chemical geodynamics. *Annu. Rev. Earth Planet. Sci.* **1986**, *14*, 493–571. [CrossRef]
46. Müller, D.; Groves, D.I. *Potassic Igneous Rocks and Associated Gold-Copper Mineralization*; Springer: Berlin, Germany, 2000; Volume 252.
47. Müller, D.; Rock, N.; Groves, D. Geochemical discrimination between shoshonitic and potassic volcanic rocks in different tectonic settings: A pilot study. *Miner. Pet.* **1992**, *46*, 259–289. [CrossRef]
48. Peccerillo, A. Potassic and ultrapotassic rocks: Compositional characteristics, petrogenesis and geologic significance. *Episodes* **1992**, *15*, 243–251.
49. Foley, S.F.; Wheller, G.E. Parallels in the origin of the geochemical signatures of island arc volcanics and continental potassic igneous rocks: The role of residual titanates. *Chem. Geol.* **1990**, *85*, 1–18. [CrossRef]
50. Sajona, F.G.; Maury, R.C.; Bellon, H.; Cotten, J.; Defant, M. High Field Strength Element Enrichment of Pliocene—Pleistocene Island Arc Basalts, Zamboanga Peninsula, Western Mindanao (Philippines). *J. Pet.* **1996**, *37*, 693–726. [CrossRef]
51. Fitton, J.G.; James, D.; Leeman, W.P. Basic magmatism associated with late Cenozoic extension in the western United States: Compositional variations in space and time. *J. Geophys. Res. Solid Earth* **1991**, *96*, 13693–13711. [CrossRef]
52. Pearce, J.A. Role of the sub-continental lithosphere in magma genesis at active continental margins. In *Continental Basalts and Mantle Xenoliths*; Hawkesworth, C.J., Norry, M.J., Eds.; Shiva Publications: Nantwich, UK, 1983; pp. 230–249.
53. Condie, K.C. Geochemical changes in baslts and andesites across the Archean-Proterozoic boundary: Identification and significance. *Lithos* **1989**, *23*, 1–18. [CrossRef]
54. Berberian, M.; King, G. Towards a paleogeography and tectonic evolution of Iran: Reply. *Can.J. Earth Sci.* **1981**, *18*, 1764–1766. [CrossRef]
55. Mohajjel, M.; Fergusson, C.; Sahandi, M. Cretaceous–Tertiary convergence and continental collision, Sanandaj–Sirjan zone, western Iran. *J. Asian Earth Sci.* **2003**, *21*, 397–412. [CrossRef]
56. Shahabpour, J. Island-arc affinity of the Central Iranian volcanic belt. *J. Asian Earth Sci.* **2007**, *30*, 652–665. [CrossRef]
57. Henderson, P. *Rare Earth Element Geochemistry*; Elsevier Science: New York, NY, USA, 1984; pp. 652–665.
58. McKenzie, D.; O'nions, R. Partial melt distributions from inversion of rare earth element concentrations. *J. Pet.* **1991**, *32*, 1021–1091. [CrossRef]
59. Furman, T.; Graham, D. Erosion of lithospheric mantle beneath the East African Rift system: Geochemical evidence from the Kivu volcanic province. *Lithos* **1999**, *48*, 237–262. [CrossRef]
60. Wilson, B.M. *Igneous Petrogenesis a Global Tectonic Approach*; Springer: Berlin, Germany, 2007.
61. Dilek, Y.; Imamverdiyev, N.; Altunkaynak, Ş. Geochemistry and tectonics of Cenozoic volcanism in the Lesser Caucasus (Azerbaijan) and the peri-Arabian region: Collision-induced mantle dynamics and its magmatic fingerprint. *Int. Geol. Rev.* **2010**, *52*, 536–578. [CrossRef]
62. Aydin, F.; Karsli, O.; Chen, B. Petrogenesis of the Neogene alkaline volcanics with implications for post-collisional lithospheric thinning of the Eastern Pontides, NE Turkey. *Lithos* **2008**, *104*, 249–266. [CrossRef]
63. Sun, S.-S.; McDonough, W.-S. Chemical and isotopic systematics of oceanic basalts: Implications for mantle composition and processes. *Geol. Soc. Lond. Spec. Publ.* **1989**, *42*, 313–345. [CrossRef]
64. Widdowson, M.; Pringle, M.; Fernandez, O. A post K–T boundary (Early Palaeocene) age for Deccan-type feeder dykes, Goa, India. *J. Pet.* **2000**, *41*, 1177–1194. [CrossRef]
65. Moayyed, M. Petrologic Studies of Tertiary Volcano-Plutonic Belt in Western Alborz-Azerbaijan, with a Special Focus on Hashtchin Area, Iran. Ph.D. Thesis, University of Shahid Beheshti, Tehran, Iran, 2001.

66. Sheikholeslami, M.R.; Piqu, A.; Mobayen, E.P.; Sabzehi, M.; Bellon, H.; Emami, M.H. Tectono–metamorphic evolution of the Neyriz metamorphic complex, Quri–Kor–e Sefid area (Sanandaj–Sirjan Zone, SW Iran). *J. Asian Earth Sci.* **2008**, *31*, 504–521. [CrossRef]
67. Agard, P.; Monie, P.; Gerber, W.; Omrani, J.; Molinaro, M.; Meyer, B.; Labrousse, L.; Jolivet, L.; Yamato, P. Transient, synobduction exhumation of Zagros blueschists inferred from P–T, deformation time and kinematic constraints: Implications for Neotethyan wedge dynamics. *Geophys. Res.* **2006**, *111*, 11401. [CrossRef]
68. Alavi, M. Tectono-stratigraphic syntethesis and structural style of the Alborz mountain system in northern Iran. *J. Geodyn.* **1996**, *21*, 1–33. [CrossRef]
69. Alavi, M. Regional stratigraphy of the Zagros fold thrust belt of Iran and its proforland evolution. *Am. J. Sci.* **2004**, *304*, 1–20. [CrossRef]
70. Mohajjel, M.; Fergusson, C.L.; Sahandi, M.R. Deformation history, micro-structure and P-T-t path in ALS-bearing schists, southeast Hamaan, Sanandaj-Sirjan zone, Iran. *J. Geol. Soc. Iran* **2006**, *1*, 11–19.
71. Mehdipour Ghazi, J.; Moazzen, M.; Rahgoshay, M.; Shafaii Moghadam, S. Geochemicl characterstics of basaltic rocks from the Nain ophiolite (Central Iran): Constraints on mantle wedge source evolution in an oceanic back arc basin and a geodynamical model. *Tectonophysics* **2012**, *574–575*, 92–104. [CrossRef]
72. Aldanmaz, E.; Pearce, J.A.; Thirlwall, M.F.; Mitchell, J.G. Petrogenetic evolution of late Cenozoic, post-collision volcanism in western Anatolia, Turkey. *J. Volcanol. Geotherm. Res.* **2000**, *102*, 67–95. [CrossRef]
73. Hofmann, A.W.; Jochum, K.P.; Seufert, M.; White, W.M. Nb and Pb in oceanic basalts: New constraints on mantle evolution. *Earth Planet. Sci. Lett.* **1986**, *79*, 33–45. [CrossRef]
74. Hofmann, A. Mantle geochemistry: The message from oceanic volcanism. *Nature* **1997**, *385*, 219. [CrossRef]
75. Hofmann, A.W. Chemical differentiation of the Earth: The relationship between mantle, continental crust, and oceanic crust. *Earth Planet. Sci. Lett.* **1988**, *90*, 297–314. [CrossRef]
76. Bradshaw, T.; Smith, E.I. Polygenetic Quaternary volcanism at Crater Flat, Nevada. *J. Volcanol. Geotherm. Res.* **1994**, *63*, 165–182. [CrossRef]
77. Smith, E.I.; Sanchez, A.; Walker, J.D.; Wang, K. Geochemistry of mafic magmas in the Hurricane Volcanic field, Utah: Implications for small-and large-scale chemical variability of the lithospheric mantle. *J. Geol.* **1999**, *107*, 433–448. [CrossRef]
78. Chen, W.; Arculus, R. Geochemical and isotopic characteristics of lower crustal xenoliths, San Francisco Volcanic Field, Arizona, USA. *Lithos* **1995**, *36*, 203–225. [CrossRef]
79. Weaver, B.L.; Wood, D.A.; Tarney, J.; Joron, J.L. Geochemistry of ocean island basalts from the south Atlantic: Ascension, Bouvet, St. Helena, Gough and Tristan da Cunha. *Geol. Soc. Lond. Spec. Publ.* **1987**, *30*, 253–267. [CrossRef]
80. Haase, K.M.; Mühe, R.; Stoffers, P. Magmatism during extension of the lithosphere: Geochemical constraints from lavas of the Shaban Deep, northern Red Sea. *Chem. Geol.* **2000**, *166*, 225–239. [CrossRef]
81. Menzies, M.A.; Kyle, P.R.; Jones, M.; Ingram, G. Enriched and depleted source components for tholeiitic and alkaline lavas from Zuni-Bandera, New Mexico: Inferences about intraplate processes and stratified lithosphere. *J. Geophys. Res. Solid Earth* **1991**, *96*, 13645–13671. [CrossRef]
82. Abdel-Rahman, A.F.; Nassar, P.E. Cenozoic volcanism in the Middle East: Petrogenesis of alkali basalts from northern Lebanon. *Geol. Mag.* **2004**, *141*, 545–563. [CrossRef]